

Oligodendrocyte precursor cells prune axons in the mouse neocortex

JoAnn Buchanan (✉ joannb@alleninstitute.org)

Allen Institute for Brain Sciences

Leila Elabbady

Allen Institute for Brain Science

Forrest Collman

Allen Institute for Brain Science

Nicholas Jorstad

Allen Institute for Brain Science

Trygve Bakken

Allen Institute for Brain Science <https://orcid.org/0000-0003-3373-7386>

Carolyn Ott

Janelia Research Campus HHMI

Jenna Glazer

Johns Hopkins University School of Medicine

Adam Bleckert

Allen institute for Brain Science

Agnes Bodor

Allen Institute for Brain Science

Derrick Brittain

Allen Institute for Brain Science

Dan Bumbarger

Allen Institute

Gayathri Mahalingam

Allen Institute for Brain Science

Sharmishta Seshamani

Allen Institute for Brain Science

Casey Schneider-Mizell

Allen Institute for Brain Science

Marc Takeno

Allen Institute for Brain Science <https://orcid.org/0000-0002-8384-7500>

Russel Torres

Allen Institute for Brain Science <https://orcid.org/0000-0002-2876-4382>

Wenjing Yin

Allen institute for Brain Science

Rebecca Hodge

Allen Institute for Brain Science <https://orcid.org/0000-0002-5784-9668>

Manuel Castro

Princeton University <https://orcid.org/0000-0003-2787-0332>

Sven Dorkenwald

Princeton University

Dodam Ih

Princeton University

Chris Jordan

WiredDifferently, Inc.

Nico Kemnitz

Princeton University

Kisuk Lee

Massachusetts Institute of Technology

Ran Lu

Princeton University

Thomas Macrina

Princeton University <https://orcid.org/0000-0002-0622-9338>

Shang Mu

Princeton University

Sergiy Popovych

Princeton University

William Silversmith

Princeton University

Ignacio Tartavull

Princeton University

Nicholas Turner

Princeton University

Alyssa Wilson

Princeton University

William Wong

Princeton University

Jingpeng Wu

Princeton University

Aleksandar Zlateski

Princeton University

Jonathan Zung

Princeton University

Jennifer Lippincott-Schwartz

Janelia Research Campus, Howard Hughes Medical Institute, Ashburn, VA, 20147

<https://orcid.org/0000-0002-8601-3501>

Ed S. Lein

Allen Institute for Brain Science <https://orcid.org/0000-0001-9012-6552>

H. Sebastian Seung

Princeton University <https://orcid.org/0000-0002-8591-6733>

Dwight Bergles

Johns Hopkins University <https://orcid.org/0000-0002-7133-7378>

R. Clay Reid

Allen Institute for Brain Science <https://orcid.org/0000-0002-8697-6797>

Nuno da Costa

Allen Institute for Brain Science

Biological Sciences - Article

Keywords: serial electron microscopy, glial types, visual cortex, oligodendrocyte precursor cells

Posted Date: June 29th, 2021

DOI: <https://doi.org/10.21203/rs.3.rs-581121/v1>

License:  This work is licensed under a Creative Commons Attribution 4.0 International License.

[Read Full License](#)

1 **Oligodendrocyte precursor cells prune axons in the mouse neocortex**

2
3 JoAnn Buchanan^{1,7*}, Leila Elabbady¹, Forrest Collman¹, Nikolas L. Jorstad¹, Trygve E.
4 Bakken¹, Carolyn Ott², Jenna Glatzer³, Adam A. Bleckert¹, Agnes L. Bodor¹, Derrick Brittan¹,
5 Daniel J. Bumbarger¹, Gayathri Mahalingam¹, Sharmishta Seshamani¹, Casey Schneider-
6 Mizell¹, Marc M. Takeno¹, Russel Torres¹, Wenjing Yin¹, Rebecca D. Hodge¹, Manuel Castro⁴,
7 Sven Dorkenwald^{4,5}, Dodam Ih⁴, Chris S. Jordan⁴, Nico Kemnitz⁴, Kisuk Lee^{4,5}, Ran Lu⁴,
8 Thomas Macrina⁴, Shang Mu⁴, Sergiy Popovych⁵, William M. Silversmith⁵, Ignacio Tartavull⁵,
9 Nicholas L. Turner^{4,5}, Alyssa M. Wilson⁴, William Wong⁴, Jingpeng Wu⁴, Aleksandar Zlateski⁴,
10 Jonathan Zung⁴, Jennifer Lippincott-Schwartz², Ed S. Lein¹, H. Sebastian Seung^{4,5}, Dwight E.
11 Bergles^{3,6}, R. Clay Reid¹, Nuno Maçarico da Costa^{1,7*}

12
13 ¹Allen Institute for Brain Sciences

14
15 ²Janelia Research Campus, Howard Hughes Medical Institute

16
17 ³The Solomon H. Snyder Department of Neuroscience, John Hopkins University School of
18 Medicine

19
20 ⁴Princeton Neuroscience Institute, Princeton University

21
22 ⁵Computer Science Department, Princeton University

23
24 ⁶Johns Hopkins Kavli Neuroscience Discovery Institute

25
26 ⁷Corresponding Authors

27
28
29

30 **ABSTRACT**

31 Neurons in the developing brain undergo extensive structural refinement as nascent circuits adopt
32 their mature form¹. This transformation is facilitated by the engulfment and degradation of excess
33 axonal branches and inappropriate synapses by surrounding glial cells, including microglia and
34 astrocytes^{2,3}. However, the small size of phagocytic organelles and the complex, highly ramified
35 morphology of glia has made it difficult to determine the contribution of these and other glial cell
36 types to this process. Here, we used large scale, serial electron microscopy (ssEM) with
37 computational volume segmentation to reconstruct the complete 3D morphologies of distinct glial
38 types in the mouse visual cortex. Unexpectedly, we discovered that the fine processes of
39 oligodendrocyte precursor cells (OPCs), a population of abundant, highly dynamic glial
40 progenitors⁴, frequently surrounded terminal axon branches and included numerous
41 phagolysosomes (PLs) containing fragments of axons and presynaptic terminals. Single- nucleus
42 RNA sequencing indicated that cortical OPCs express key phagocytic genes, as well as neuronal
43 transcripts, consistent with active axonal engulfment. PLs were ten times more abundant in OPCs
44 than in microglia in P36 mice, and declined with age and lineage progression, suggesting that
45 OPCs contribute very substantially to refinement of neuronal circuits during later phases of
46 cortical development.

47

48 **MAIN**

49 OPCs emerge from several germinal zones in late prenatal development following the sequential
50 generation of neurons and astrocytes, migrate into the expanding cortex and then proliferate to
51 establish a grid-like distribution, with individual cells occupying distinct territories. Genetic fate
52 tracing and time lapse imaging *in vivo* have demonstrated that these progenitors play a critical role
53 in generating oligodendrocytes and thus myelin throughout the central nervous system (CNS)⁵.
54 However, OPCs are present in some cortical regions weeks before oligodendrogenesis begins and
55 extend highly ramified processes that developing neurons. These progenitors express a diverse set
56 of neurotransmitter receptors and form direct, functional synapses with excitatory and inhibitory
57 neurons.^{6,7} These features have traditionally been viewed through the perspective of
58 oligodendrogenesis⁸, as other functions for these ubiquitous glial cells have not been clearly
59 established. Our knowledge about the structure and function of OPCs has been severely limited by
60 incomplete ultrastructural information, because their fine, highly branched processes are difficult

61 to unambiguously identify in EM studies without complete reconstructions to connect them to
62 identifiable somata. Modern computational volume EM methods offer new opportunities to
63 increase our understanding of brain ultrastructure⁹⁻¹², particularly for morphologically complex,
64 highly dynamic glial cells like OPCs. Here, we used two densely segmented and reconstructed
65 datasets of mouse visual cortex, ages P36 (Fig. 1a) and P49, to perform a detailed morphometric
66 analysis and quantification of the anatomical features of somata, processes, and organelles of OPCs
67 at this highly dynamic phase of neocortical maturation to help define their roles in the developing
68 brain.

69

70 **Structural features of OPCs revealed by large scale serial EM**

71 Past EM ultrastructural studies defined several common morphological characteristics of OPCs,
72 such as their bean-shaped nucleus containing low heterochromatin and presence of centrioles in
73 their cytoplasm¹³, consistent with their proliferative progenitor state.¹⁴ Originally referred to as a
74 multipotential type of glia⁴, and often described as NG2 cells^{15,16} in reference to their expression
75 of the proteoglycan NG2, early EM investigations often focused on their cellular responses to
76 injury and the close association of their processes with synapses and degenerating nerve fibres^{15,17}.
77 More recent studies indicate that OPC processes form direct synapses with axons and that OPCs
78 contact nodes of Ranvier^{6,18} in naïve animals; however, quantitative analysis of these structural
79 features has been difficult due to the limited sampling^{6,15,17,18}.

80

81 The two EM volumes P36 (Fig. 1.a) and P49 we examined in serial sections contained four distinct
82 classes of glia: OPCs (Fig. 1b, c), microglia (Fig. 1d), oligodendrocytes (Fig.1e), and astrocytes
83 (Fig. 1f). OPCs exhibited a ramified form with 15 to 17 highly branched processes extending up
84 to 50 μm radially from the soma (Fig. 1b, c, g, h, Extended Data Fig.1 c-j) that contained numerous
85 filopodia on their tips. 3D renderings of multiple cells revealed that OPCs, similar to astrocytes
86 and microglia^{19,20}, formed a grid-like organization with little overlap between territories of
87 adjacent cells of the same class (Fig. 1b), and also contacted synapses^{21,22}. The OPC somata were
88 frequently in a satellite position, like those of microglia and oligodendrocytes^{23,24} (Fig. 1g,
89 Extended Data Fig. 1c-k; Video 1), and were remarkably variable in both size and shape, ranging
90 from elongated or bean shaped to smooth or irregular with a rough surface (Fig. 1b; Extended Data
91 Fig. 1c-j). OPCs were readily distinguished from other glial cell types by these features as well as

92 having: 1) larger nuclei that were elongated and contained less heterochromatin than those of
93 microglia (Fig. 1i-k); 2) processes that were longer and smoother compared to microglia or
94 astrocytes (Fig. 1c, d, f); 3) axons that formed synaptic contacts with their processes (Fig. 1l, m);
95 4) cytoplasm that was more electron lucent than that of microglia and devoid of glycogen granules
96 that are numerous in astrocytes (Fig. 1m); and 5) the presence of primary cilia, which were not
97 found in microglia, pre-myelinating or mature oligodendrocytes (Fig. 1n,o; Extended Data Fig.
98 1c-j,1k).

99

100 **OPC processes contain numerous lysosomes and phagolysosomes**

101 Previous *in vivo* imaging experiments revealed the dynamic nature of OPC processes, which
102 exhibit continuous branch remodeling as they migrate through the gray matter, making transient
103 interactions with various cellular constituents²⁵. Based on profiles in EM images and associated
104 cellular reconstructions, we find that OPC processes were often found in contact with axons
105 (Fig.2a-d). Unexpectedly, the cytoplasm of these processes often contained numerous membrane-
106 bound organelles that included phagosomes and primary and secondary lysosomes, termed
107 phagolysosomes(PLs)(Fig. 2b,c,e), suggesting that OPCs at this age are engaging in phagocytosis.
108 The process of phagocytosis begins with recognition of a target, followed by phagosome formation
109 (engulfment) and maturation, and then fusion of the phagosome with a lysosome, forming a PL²⁶.
110 In both EM volumes, phagosomes were identified as completely internalized, membrane delimited
111 structures. Lysosomes appeared electron dense and measured ~ 500 nm in diameter (Fig. 2b), while
112 PLs were multichambered, large organelles measuring ~ 750 nm (Fig. 2e-n). Seldom visualized in
113 large numbers by EM, PLs represents the final step of phagocytosis, and constitute a highly acidic
114 compartment capable of destroying ingested elements^{26,27}. Mapping the distribution of PLs in one
115 OPC (Fig. 2o) demonstrated that they were widely distributed within the cell, but particularly
116 prevalent near the tips of OPC processes. This finding led us to count PLs in eight more OPCs in
117 P36 dataset for comparison.

118

119 PLs in OPCs were large enough to visualize their internal contents. Although much of this material
120 was unidentifiable cellular debris, they frequently contained clusters of small (~ 40 nm), clear
121 vesicles (Fig. 2 f,i-n), suggesting that OPCs had engulfed portions of presynaptic terminals.
122 Occasionally, there was evidence of an entire synaptic terminal surrounded by OPC cytoplasm,

123 with both presynaptic vesicles and a post-synaptic density visible (Fig. 2 f,g). Notably, fragments
124 of myelin, distinct organelles (e.g. mitochondria), and cytoskeletal elements, were not observed in
125 these PLs, suggesting that OPCs primarily engulf axonal processes. In contrast, although
126 microglial PLs also contained unidentifiable electron dense material, they did not contain 40 nm
127 vesicles (Extended Data Fig. 2b-e, h), suggesting that, at this age, these two glial cell types
128 recognize and remove distinct cellular elements. The presence of abundant PLs in OPCs containing
129 synaptic material was unexpected, as most structural pruning of neurons is thought to be mediated
130 by microglia^{2,28}. To determine the relative abundance of PLs in these two glial cell types, we
131 quantified PLs in complete 3D reconstructions of microglia in the same volumes. This analysis
132 revealed that PLs were significantly more abundant in OPCs than microglia at this age (Fig.
133 2o,p; Extended Data Fig. 2) (Total PLs/cell: OPCs, 108 ± 48 ; microglia, 9 ± 3 ; student's t-test, $p <$
134 0.001 , $n = 9$); although OPCs are larger than microglia, the density of PLs was still significantly
135 higher in OPCs (Fig. 2q; Extended data Fig. 2f,g) (PL density: OPCs, 0.143 ± 0.05 PLs/ μm^3 ;
136 microglia, 0.03 ± 0.01 PLs/ μm^3 ; $p < 0.001$, $n = 9$), suggesting that OPCs are more actively engaged
137 in neuronal process engulfment at this age.

138

139 To further explore the prevalence of these organelles in OPCs, OPCs isolated from the visual
140 cortex of one month-old mice were immunolabeled for lysosomal associated membrane protein 2
141 (LAMP-2), which is associated with both lysosomes and phagolysosomes²⁹, and NG2 (chondroitin
142 sulfate proteoglycan 4) that specifically labels OPCs¹⁵. Consistent with the ultrastructural
143 observations described above, OPCs at this age contained 25 to 54 LAMP-2 immunoreactive
144 circular organelles distributed throughout their somata and processes (Extended Data Fig.1a,b),
145 indicating a high investment in cellular turnover in the developing cortex.

146

147 During the critical period of mouse visual cortex from P21 to P35, microglia engulf and eliminate
148 synapses^{30,31} and neuronal corpses through phagocytosis and eventual digestion via acidified
149 phagosomes and PLs³². This structural remodeling of cortical connections declines rapidly after
150 the first postnatal month^{2,33}, coinciding with the end of the critical period of ocular dominance
151 plasticity in the visual cortex. To determine if PLs in OPCs follow a similar developmental
152 progression, we quantified PLs in OPCs reconstructed from serial EM volumes obtained in the
153 P49 mouse visual cortex. Significantly fewer PLs were present in OPCs at this age, despite the

154 similar volume occupied by these cells (Extended Data Fig. 3e, f, g) (PL density: P36 OPCs, 0.143
155 ± 0.05 PLs/ μm^3 ; P49 OPCs, 0.085 ± 0.03 PLs/ μm^3 ; $p = 0.01$, student's t-test, $n = 9, 11$,
156 respectively). Together, these results indicate there is a temporal shift in OPC behavior over time
157 and that OPCs may contribute to an early phase of structural remodeling of neurons during the
158 final phase of the critical period in the visual cortex.

159

160 OPCs undergo dramatic changes in gene expression and morphology as they differentiate into
161 myelin forming oligodendrocytes⁸ (Extended Data Fig. 3a-d). To determine if axonal engulfment
162 is preferentially associated with the OPC progenitor state, we also examined the cytosol of
163 premyelinating and mature oligodendrocytes at P49 (due to the smaller volume, there was only
164 one partially reconstructed premyelinating oligodendrocyte in the P36 dataset). These more mature
165 oligodendroglia were distinguished from OPCs by the lack of primary cilia³⁴, as well as the
166 presence of sheets of membrane extending along axons and membrane wraps indicative of nascent
167 myelination (Extended Data Fig. 3a-d). Premyelinating oligodendrocytes had lower densities of
168 PLs than OPCs PL density: P49 OPCs, 0.085 ± 0.03 PLs/ μm^3 ; P49 Pre-myelinating
169 oligodendrocyte, 0.034 ± 0.018 PLs/ μm^3 ; $p = 0.001$, student's t-test, $n = 11, 5$,
170 respectively,(Extended Data Fig. 3f). In fully mature oligodendrocytes, PLs were extremely rare
171 (extended figure 3.e), suggesting that engulfment of neuronal processes declines rapidly as OPCs
172 undergo differentiation (Extended Data, Fig. 3e, f, g).

173

174 **OPCs express genes that enable phagocytosis**

175 The 3D EM reconstructions indicate that OPC processes are filled with numerous PLs that contain
176 neuronal material, suggesting that they assist in remodeling nascent neuronal circuits through
177 engulfment of axons and synapses. Phagocytosis requires a complex array of proteins to recognize
178 and engulf distinct cargos, the components for which are highly conserved among different
179 species. To determine whether OPCs express genes that would enable this behavior, we analyzed
180 existing single nucleus RNA-seq and DNA-methylation data sets derived from the mouse motor
181 cortex (P56)³⁵ for both lysosomal and phagocytic genes (Fig. 3a,b). OPC nuclei were identified by
182 co-expression of *pdgfra* and *olig2* and premyelinating/myelinating oligodendrocytes were
183 identified by expression of *opalin*(Fig.3 a-c). Expression of genes that encode components of
184 phagocytosis were then compared between OPCs, microglia and mature oligodendrocytes

185 (Fig.3a,b), identified by previous characterization³⁵ and expression of distinct marker genes
186 (Extended Data Figure 4).

187
188 Both OPCs and microglia expressed high levels of mRNAs encoding phagocytic and lysosomal
189 genes. Of the 38 phagocytosis-related genes examined, 32% were expressed in OPCs and 89%
190 were expressed by microglia (Fig.3b). Eight phagocytic genes were expressed in both glial types,
191 including *Mertk*, *Ptpnj*, and *Lrp1*. *Mertk* (Mer tyrosine kinase) is a member of the TAM (Tyro3-
192 Axl-Mer) family of receptors that signal engulfment, which astrocytes use to refine connectivity
193 in the adult mouse hippocampus by phagocytosing excitatory synapses³⁶. *Ptpnj* is a tyrosine
194 phosphatase receptor protein that is known to regulate phagocytosis and migration in microglia³⁷,
195 and *Lrp1* is a low density lipoprotein receptor essential for myelin phagocytosis and regulation of
196 inflammation in OPCs³⁸. Several genes that encode phagocytosis-related proteins expressed in
197 OPCs were absent from microglia: *Rap1gap*, a GTPase activating protein that mediates FcγR
198 dependent phagocytosis³⁹; and *Xrkr4* and *Xrkr6*, proteins that promote the exposure of
199 phosphatidylserine to produce “eat me” signaling during phagocytosis, which are highly expressed
200 in the developing brain⁴⁰. The distinct complement of phagocytic genes expressed by OPCs and
201 microglia may enable these cells to identify and engulf discrete parts of neurons. Notably,
202 expression of all the phagocytosis-related genes were negligible in oligodendrocytes, consistent
203 with the much higher incidence of PLs in OPCs.

204
205 We also searched for the presence of neuronal transcripts within microglia and OPCs that may
206 have been engulfed along with neuronal processes. Neuronal transcripts were found in both OPCs
207 and microglia, which suggests both types of glia are phagocytosing neurons at this age Fig.3c,d).
208 However, transcripts encoding these components were higher in OPCs, which correlates with the
209 increased number of PLs in these cells. Because OPCs express many proteins characteristic of
210 neurons, such as AMPA and NMDA glutamate receptors and voltage-dependent Na⁺ channels, we
211 assessed the likelihood that transcription of traditionally “neuronal” genes is occurring directly in
212 OPCs by examining the methylation state of the neuronal genes; genes that are actively transcribed
213 should be hypomethylated. This analysis revealed that microglia and OPCs lack hypomethylation
214 at most neuronal genes (Fig. 3e), a sign that they do not express these genes but incorporated them
215 from elsewhere, likely by phagocytosis of neuronal material. Analysis of cell specific gene

216 expression data suggest that OPCs ingest material from diverse neurons, rather than targeting a
217 specific subtype. These findings, together with the ultrastructural data, provide further evidence
218 that OPCs phagocytose axons of many types of neurons in the mammalian cortex.

219

220 **OPCs prune axons in the mouse cortex**

221 The appearance of clusters of 40 nm clear vesicles inside OPC PLs suggests that presynaptic
222 terminals or portions of axons containing terminals are engulfed by these cells. If this process is
223 frequent, OPCs engaged in various stages of this process should be visible in the EM datasets.
224 Indeed, 3D reconstructions revealed that terminal branches of axon collaterals were often
225 surrounded by OPC processes (Fig. 4a-f). The complex anatomy of the branches and the need to
226 accurately manually annotate and quantify the ingestions, made this analysis particularly
227 challenging. Therefore, two individual main branches from two distinct OPCs in the P36 dataset
228 were examined in detail (OPCs #1, #7) (Extended Data Fig. 1c,k; Extended data Fig. 6a-h). We
229 categorized the ingestions as phagosomes (PS), PLs or axon engulfment (Fig. 4g). For the latter,
230 there was no evidence of injury or destruction to the axon, only local contact with OPC cytoplasmic
231 processes that encased the collateral or terminal region of the axon branch. Two types of axon
232 engulfment were observed: either small axonal pieces less than 1 μm in length were surrounded
233 by an OPC process, in which the collateral or terminal axon branch remained connected to the
234 parent axon (24 of 37 in OPC #1, 23 of 32 in OPC #7), or larger axonal collateral or terminal
235 branch segments (up to 3 μm) were ensheathed (9 of 37, OPC #1 and 3 of 32 OPC #7), but remained
236 attached to the parent axon (Fig. 4b,e; Extended Data Fig. 4a-h; Video 3).

237

238 OPCs form synapses with both excitatory and inhibitory neurons in the developing cortex^{6,7} and
239 axons from both neuron classes are targeted for myelination in the cortex^{41,42}, indicating that OPCs
240 and their subsequent later developmental stages interact with distinct cell types. To determine if
241 axon pruning is specific to one class of neurons, we traced the branches of 70 axons ensheathed
242 by OPCs back to the main axon and examined the boutons, classifying them as excitatory or
243 inhibitory based on synaptic morphology. This analysis showed the predominant type of axons
244 within the two isolated branches of OPCs were excitatory (89 % in OPC #1 and 81% in OPC #7
245 of ensheathed structures) (Fig. 4h,i) with 8% undetermined. Approximately 3 % of the engulfed
246 axons were identified as inhibitory, suggesting that OPCs were mainly removing portions of

247 excitatory axons, which comprise the majority of axons in cortical gray matter. This number may
248 be lower than the 10-20% inhibitory neuron population in the neocortex⁽⁴³⁾, because the sample
249 size was limited to layer 2/3 and only 2 OPC branches. Furthermore, the transcriptomics data
250 suggests that OPCs are non-discriminatory phagocytes and engulf all neuron types, based on all
251 layers of the cortex. The association of OPCs with terminal and collateral axon branches was
252 observed in all OPCs from both P36 and P49 datasets, indicating that axon pruning is a conserved
253 function of OPCs during this period. Such associations may represent the predecessor to axonal
254 engulfment and suggest that the terminal portion of axon collaterals are targeted for removal by
255 OPCs.

256

257 **Discussion**

258 Consolidation of nascent networks into stable, but adaptable, circuits requires extensive
259 remodeling during development, when excess neurons, axon collaterals and even individual
260 synapses are removed^{1,44,45}. This structural refinement is aided by glia, which recognize and engulf
261 both cellular debris and portions of intact neurons^{46,47}. Microglia are key participants in this
262 process, as they express phagocytic genes (e.g. *Merckk*, *Dock2*, *Sirpa*)⁴⁸, engage in constant
263 surveillance through process motility, can transform into amoeboid, highly phagocytic cells, that
264 accumulate presynaptic material in their cytoplasm³¹. Astrocytes also express phagocytic
265 components (e.g. *Mertk*, *Megf10*)³ and participate in excitatory synapse removal in adult mice⁴⁹,
266 indicating that structural refinement of neurons is the shared responsibility of multiple glial cell
267 types.

268

269 This new analysis of the 3D ultrastructure of individual glial cells in mouse visual cortex using
270 volumetric EM, provides strong evidence that OPCs also participate in neuronal circuit refinement.
271 OPCs, a widely distributed, and abundant population of lineage restricted progenitor cells,
272 extended fine processes that made numerous contacts with terminal axon branches and synapses
273 of excitatory neurons, surrounding and enveloping neuronal components within cup shaped and
274 sheetlike cytoplasmic formations. OPC processes contained a high density of PLs filled with
275 material exhibiting characteristic features of synapses, suggesting that OPCs target specific
276 portions of axons for removal. These ingestions could represent trogocytosis, in which small
277 portions of cells are pinched off⁵⁰. Although the molecular mechanisms that enable trogocytosis

278 have not been fully defined, OPCs expressed numerous genes involved in phagocytosis. In
279 addition, they contained DNA encoding key neuronal constituents, which due to a higher
280 methylation state are likely to have been acquired from neurons. Together, these data provide
281 evidence that OPCs not only serve as progenitors for oligodendrocytes, but also engage in the
282 pruning of neuronal processes during a robust stage of cortical alteration and maturation. By
283 leveraging multiple glial cell types, the nervous system may accelerate circuit refinement by
284 enhancing overall degradative capacity and enable greater spatial and temporal control of this
285 process by recruiting cells that recognize distinct cellular components.

286

287 Emerging evidence suggests that OPCs do more than serve as progenitors for oligodendrocytes, as
288 they are found in regions where there is no myelin, and like microglia, OPCs migrate to sites of
289 injury and contribute to scar formation⁵¹⁻⁵³. Moreover, recent evidence indicates that OPCs can
290 transform into inflammatory OPCs (*iOPCs*) that engulf and present exogenous antigens through
291 MHC class I and II when exposed to inflammatory cytokines, suggesting that they may modulate
292 tissue inflammation^{54,55}. OPCs share many other features with microglia – they are present at a
293 similar density, maintain a grid-like distribution with non-overlapping domains, possess ramified,
294 radially-oriented processes and are highly motile, continuously exploring their surrounding
295 environment with dynamic filopodia²⁵.

296

297 The robust dynamics and broad distribution of OPCs place them in an ideal position to engage in
298 the modification of neural circuits that we describe in this study. Remarkably, OPC processes
299 contained a higher density of PLs than surrounding microglia, raising the possibility that they are
300 responsible for a greater amount of pruning at this stage of maturation of the cortex. However, it
301 is also possible the engulfment and digestion of axonal elements proceeds more slowly in OPCs
302 than microglia, leading to more PL accumulation. Although the presence of PLs within OPC
303 processes declined with age, the persistence of OPCs throughout the CNS, which retain a similar
304 morphology and dynamics, raises the possibility that they may retain the capacity to modify
305 circuits and clear cellular debris induced by injury or normal aging.

306

307 Many OPCs in this region of the developing cortex will differentiate to form oligodendrocytes that
308 myelinate both excitatory and inhibitory axons^{43,56-58}. However, the interactions between neurons

309 and OPCs described here are distinct from the early stages of axon wrapping, as these cells had
310 not yet begun transforming into oligodendrocytes, and PL abundance rapidly declined with
311 differentiation. Whether the interactions described here are an early harbinger of myelination^{56,59},
312 to possibly trim superfluous axon branches prior to axon ensheathment or signal which regions of
313 axons are to be myelinated, are not yet known.

314

315 These findings raise new questions about how distinct glial cell types coordinate their phagocytic
316 behavior to shape brain connectivity and contribute to plasticity, homeostasis and disease
317 processes. Future studies selectively targeting engulfment by OPCs at different time points may
318 reveal the complex role of these progenitors in early refinement of neural circuits and explore their
319 interactions with astrocytes and microglia.

320

321

322

323

324

325

326

327

328

329

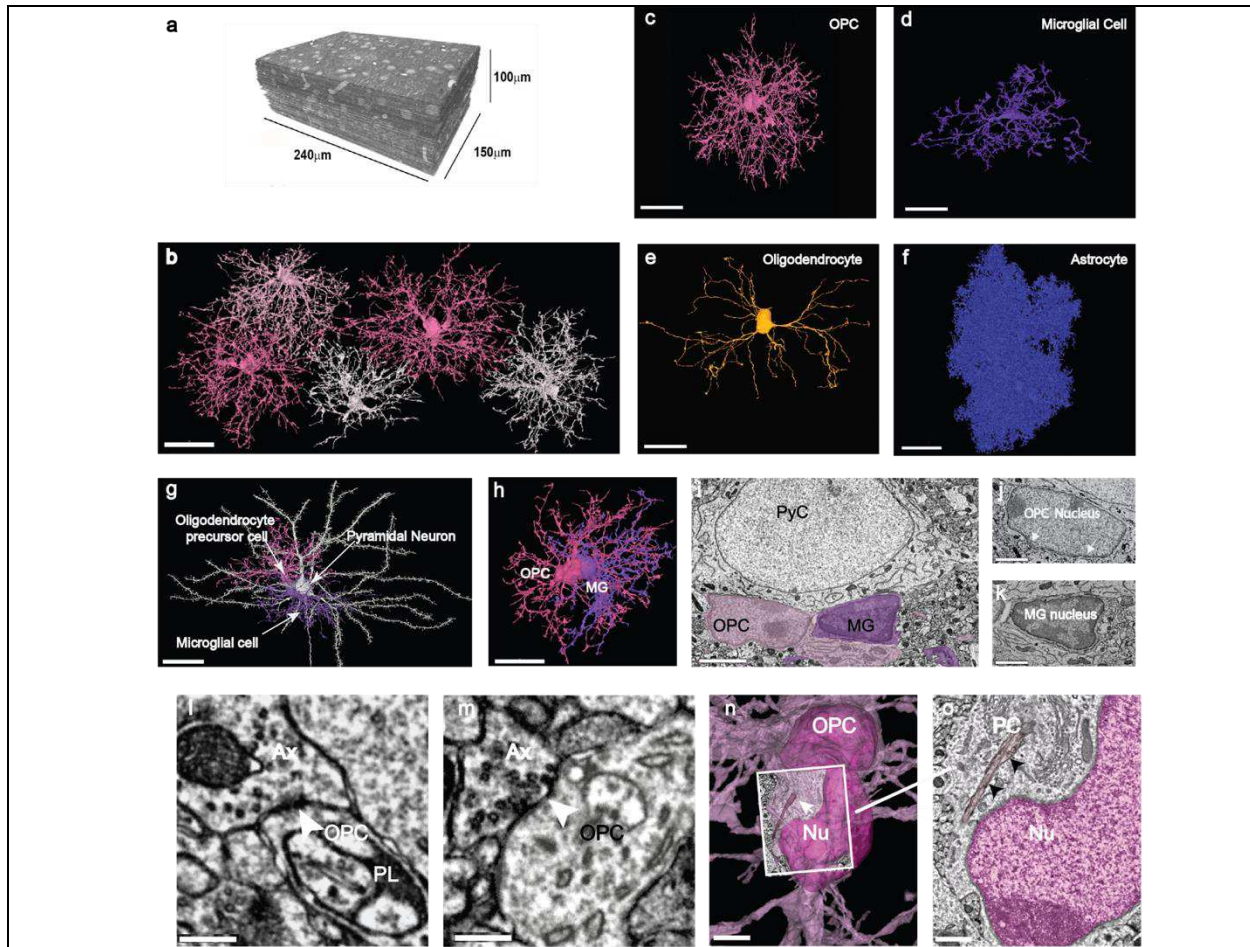


Figure 1: Distinct structural features of OPCs in the developing visual cortex.

a, ssEM reconstruction of $100 \mu\text{m}^3$ volume of layer 2/3 mouse visual cortex (P36). **b**, 3D reconstructions of a subset of OPCs in P36 dataset, showing discrete territories and tiling. Scale bar, $30 \mu\text{m}$. **c**, 3D rendering of an OPC from P36 dataset showing extensive ramifications emanating from the cell soma. **d**, 3D rendering of a microglial cell shows its shorter, less branched processes and elongated and flattened soma. **e**, 3D rendering of a mature myelinating oligodendrocyte in P36 dataset has a smooth and ovoid shaped soma. Note, only the soma and cytoplasmic processes without myelin sheaths are shown. **f**, 3D rendering of an astrocyte in P36 dataset showing its densely packed cytoplasmic protrusions. Scale bars c-f, $20 \mu\text{m}$. **g**, 3D rendered pyramidal neuron (white) with an OPC (pink) and a microglial cell (MG, purple) both in satellite positions. Scale bar, $30 \mu\text{m}$. (See also Extended Data Video 1) **h**, 3D rendering of the same two glial cells in **g** shows their close association and intermingling of branches. Scale bar, $20 \mu\text{m}$. **i**, Ultrathin section slice through an OPC soma (pink) and microglial cell soma (purple). Scale bar, $3 \mu\text{m}$. **j**, Ultrathin section slice of an OPC nucleus with dense rim of heterochromatin and ruffled edge (arrows). Scale bar, $1.5 \mu\text{m}$. **k**, Ultrathin section slice of a microglial nucleus showing its dense heterochromatin throughout. Scale bar, $1.5 \mu\text{m}$. **l-m**, Axons (Ax) making synaptic contacts with OPC processes (see also Extended Data Fig.1k). Scale bar, 300nm . **n**, The soma of an OPC (dark pink) bears a primary cilium (arrow) adjacent to the nucleus (Nu). Scale bar, $3 \mu\text{m}$. **o**, Ultrathin slice of the boxed area in **n** showing the primary cilium (PC) (arrows) close to the OPC nucleus (Nu, dark pink). Scale bar, 750nm . (See also Extended Data Video 2, for details on how to explore public data).

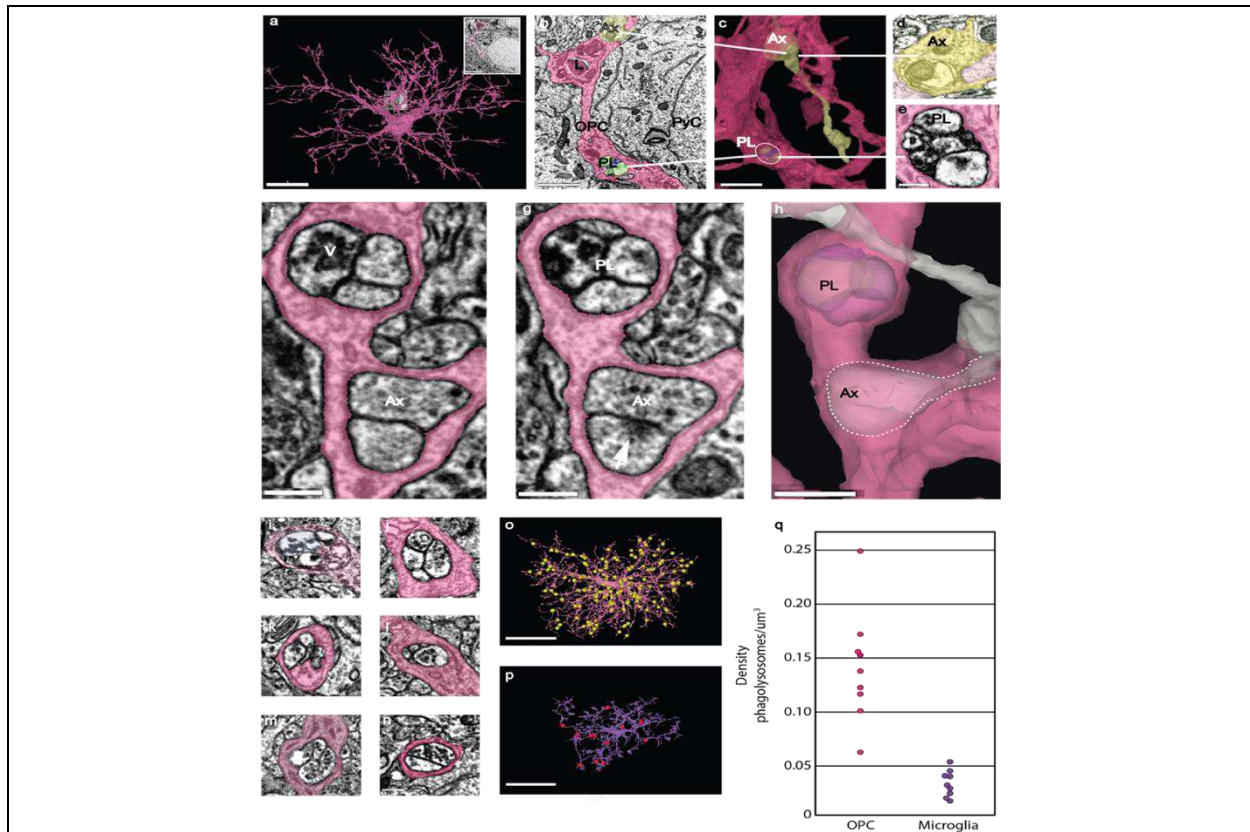


Figure 2: Phagolysosomes are abundant in OPC processes. **a**, 3D rendering of an OPC from the P36 dataset showing ramified branches. Scale bar, 15 μm . Insert shows the same area as in **b**. **b**, Ultrathin section slice of OPC branch containing a phagolysosome (PL), a lysosome (L) and an axon (Ax) passing through the OPC cytoplasm. The branch contacts the adjacent pyramidal cell (PyC). Scale bar, 1.5 μm . **c**, 3D view of the same OPC branch showing the axon (Ax) (yellow) partially encased within the OPC cytoplasm. The same phagolysosome (PL) in **2b** is visible (white circle). Scale bar, 1.5 μm . **d**, Higher magnification view of axon in **c** (yellow). Scale bar, 300 nm. **e**, Higher magnification of phagolysosome (PL) (white line) in **c** highlighting multiple chambers containing cellular debris. Scale bar, 300 nm. **f**, OPC branch from P36 dataset contains a phagolysosome with vesicles (v) and an encapsulated axon (Ax). Scale bar, 300 nm. **g**, A portion of the same branch showing the phagolysosome (PL) and post synaptic density of a synapse onto an encapsulated axon (Ax) (arrows). Scale bar, 300 nm. **h**, 3D rendering of the same branch showing both the phagolysosome (PL) and the axon encapsulated collateral within the OPC cytoplasm. Scale bar, 500 nm. **i-n**, Examples of PLs from different OPCs showing the presence of 40 nm vesicles within the chambers. Scale bar, 300 nm. **o**, 3D reconstruction of an OPC from the P36 dataset. Yellow spheres represent manual annotations of the 189 phagolysosomes found in this OPC. Scale bar, 20 μm (original data in <http://www.microns-explorer.org/phagolysosomes/opc>). **p**, 3D reconstruction of a microglial cell from the P36 dataset. Red spheres represent manual annotations of the 13 phagolysosomes present in this cell. Scale bar, 20 μm (original data in <http://www.microns-explorer.org/phagolysosomes/microglia>). **q**, Plot comparing PL density in 9 OPCs and 9 microglia in the P36 dataset.

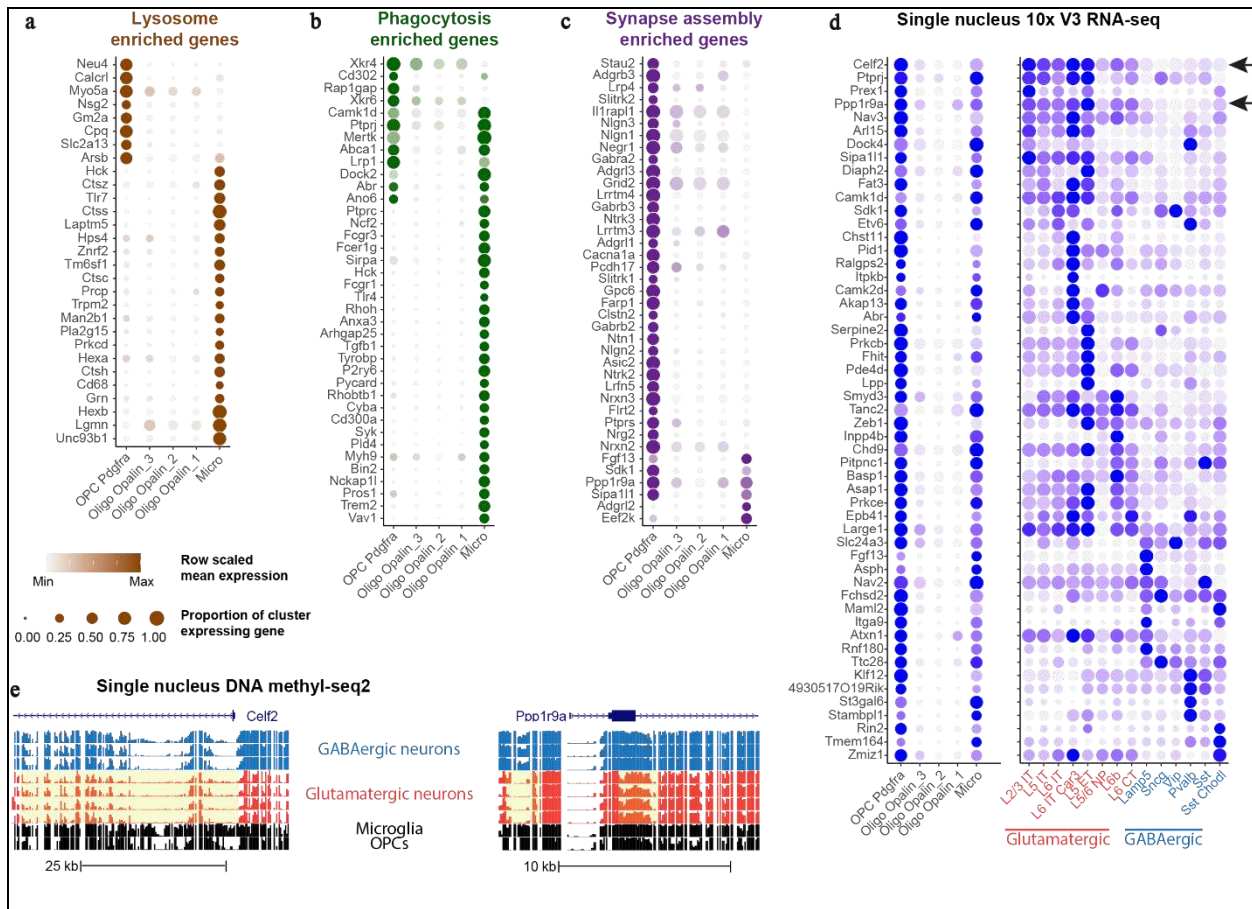


Figure 3: Detection of phagolysosome genes and neuronal transcripts in OPCs, oligodendrocytes and microglia. a-c, Dot plots of enriched lysosome (a), phagocytosis (b), and synapse assembly (c) GO term genes enriched in OPCs and/or microglia, relative to mature oligodendrocytes. d, Dot plot of neuronal subclass marker genes expressed in OPCs, mature oligodendrocytes – Oligo, microglia – Micro, and glutamatergic (red) and GABAergic (blue) neuronal subclasses. e, Genome tracks showing glutamatergic marker genes, *Celf2* (top panel) and *Ppp1r9a* (bottom panel) with hypomethylated chromatin highlighted in yellow. Blue tracks show GABAergic and red tracks show glutamatergic neuronal subclasses.

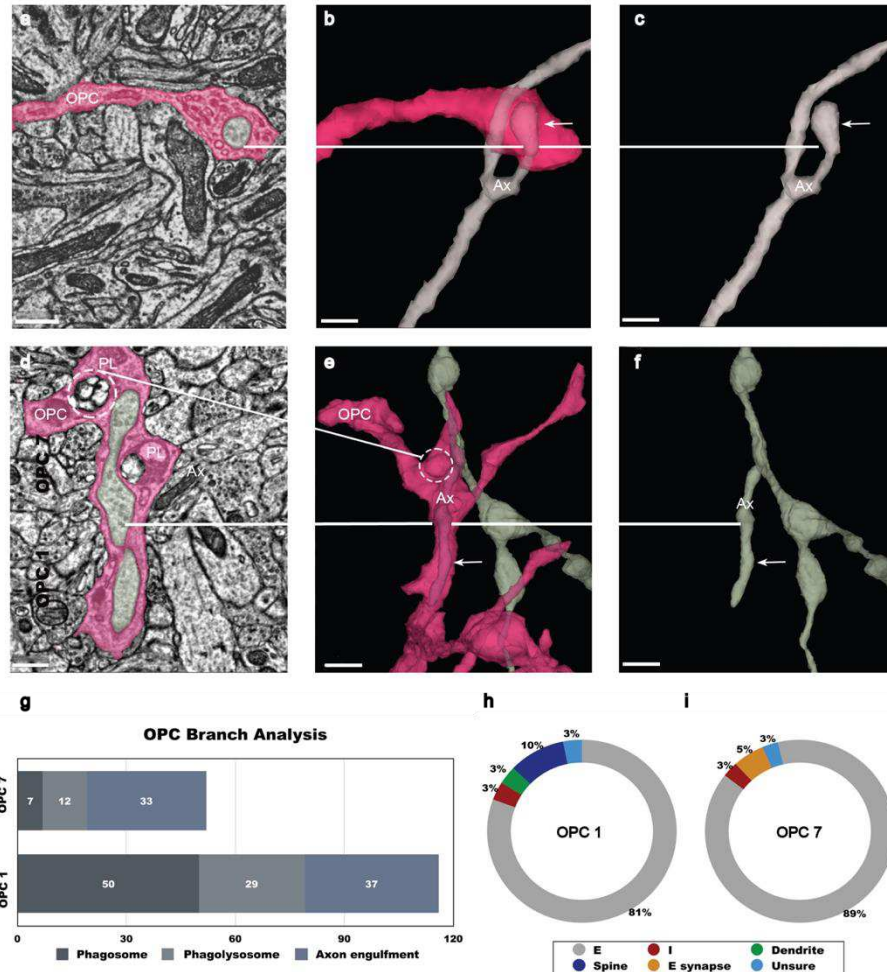


Figure 4: Axon Engulfment by OPCs. **a**, OPC process in pink ingests an excitatory axon bouton (gray) at its tip. Scale bar, 500 nm. **b**, 3D reconstruction reveals a small excitatory axon fragment (Ax) encapsulated within the OPC (pink) at the tip (white line, arrow). Scale bar, 500 nm. **c**, 3D reconstruction shows the same axon (Ax)(arrow) without OPC surrounding it. The bouton tip is visible. Scale bar, 500 nm. **d**, Ultrathin section slice of a large section of an inhibitory axon (Ax)_collateral branch (white line) in gray ingested within the cytoplasm of the OPC (pink). Two phagolysosomes (PL) (dashed circle) are adjacent to the ingested axon. Scale bar, 500 nm. **e**, 3D rendered axon collateral branch encapsulated within the cytoplasm of the OPC (arrow, white line) and phagolysosome within the cytoplasm (dashed circle). Scale bar, 1 μ m. **f**, 3D reconstruction of the axon (Ax) in gray shows encapsulated branch (white line, arrow) without the surrounding OPC. Scale bar, 1 μ m. **g**, Two individual isolated main branches (one each) of OPC cells #1 and #7 were analyzed for ingestion events. Ingestions were categorized as phagosome (PS) phagolysosome (PL) or axon collaterals engulfed in OPC cytoplasm. **h,i**, Donut charts of OPCs 1 and 7 quantifies axons partially ingested shows the types-excitatory (E) or inhibitory (I) by examination of boutons and synaptic connections and contact with other neural elements dendrite(D), spine(S), excitatory synapse(ESyn) or unsure (U). Excitatory axons ingestion was most prevalent 89% in OPC#1 and 81% in OPC#7. (See also Extended Data Video 3)

334 **Methods**

335

336 Animal procedures were approved by the Institutional Animal Care and Use Committee at the
337 Allen Institute for Brain Science or Baylor College of Medicine.

338

339 **EM Datasets**

340 We used two densely segmented and reconstructed volumes, obtained from serial section electron
341 microscopy (ssEM) in mouse primary visual cortex. These data sets were collected as part of the
342 IARPA Machine Intelligence from Cortical Network (MICrONS) consortium project
343 (<https://www.iarpa.gov/index.php/research-programs/microns>) to study the functional
344 connectivity of neurons, however they also provide in rich and unprecedented detail the fine
345 morphology of glial cell types. Here we use these datasets to evaluate the population of OPCs and
346 microglia in the 3D environment of the mouse brain visual cortex (preparation methods described
347 below). Dataset 1 was taken from a 200 μm thick sample containing layer 2/3 of mouse visual
348 cortex (P36) and measured approximately 250 μm x 140 μm x 90 μm (Fig.1A). Dataset 2 was
349 taken from a 200 μm thick sample taken from a P49 mouse visual cortex and included all 6 layers,
350 measuring approximately 56 μm x 1 mm x 30 μm . The P36 data set is publicly available at
351 <https://microns-explorer.org/>.

352

353 **Mouse line**

354 Mouse P 36 was a triple-heterozygote for the following three genes: (1) Cre driver: CAMKIIa_
355 _Cre (Jax: 005359<<https://www.jax.org/strain/005359>>), (2) tTA driver: B6;CBA- Tg(Camk2a-
356 tTA)1Mmay/J (Jax: 003010<<https://www.jax.org/strain/003010>>), (3) GCaMP6f Reporter:
357 Ai93(JAX 024103) (Allen Institute)⁶⁰. Mouse P49 was a cross of: B6;CBA-Tg(Camk2a-
358 tTA)1Mmay/J (Jax: 003010) and B6;DBA-Tg(tetO-GCaMP6s)2Niell/J (Jax: 024742).

359

360 **Two-Photon Imaging**

361 Before preparation for electron microscopy, mice underwent neurophysiology data acquisition
362 conducted at Baylor College of Medicine (details in ⁹). Note that this 2-photon data was not used
363 in this study. Briefly, a 3 mm craniotomy was made centered on the primary visual cortex (V1;
364 2.7mm lateral of the midline, contacting the lambda suture), and the cortical window was then
365 sealed with a 3 mm coverslip (Warner Instruments), using cyanoacrylate glue (VetBond). The
366 mouse was allowed to recover for 1-2 hours prior to the imaging session. Imaging was performed
367 in V1, in a 400 \times 400 \times 200 μm^3 volume with the superficial surface of the volume at the border
368 of L1 and L2/3, approximately 100 μm below the pia. Laser excitation was at 920nm at 25-45mW
369 depending on depth. The objective used was a 25x Nikon objective with a numerical aperture of
370 1.1, and the imaging point-spread function was measured with 500 nm beads and was
371 approximately 0.5 \times 0.5 \times 3 μm^3 in x, y, and z. To aid in registration of optical physiology data
372 to EM data, a wide field image of the cranial window visualizing the surface vasculature was
373 provided in addition to a volumetric image stack of the vasculature, encompassing the region of
374 tissue where the neurophysiology dataset was acquired. The vasculature was imaged by
375 subcutaneous injection of 60 μL 2.5% Texas Red 3000MW Lysine fixable (Life Technologies
376 D3328, allowing blood vessels and GCaMP6-expressing cell bodies to be imaged simultaneously
377 by 2-photon microscopy. Mice were then transferred to the Allen Institute in Seattle and kept in a
378 quarantine facility for 1 to 3 days, prior to perfusion.

379

380 **Perfusion**

381 After induction of anesthesia with isoflurane, the appropriate plane of anesthesia was checked by
382 a lack of toe pinch reflex and the animals were transcardially perfused with 15 ml 0.15 M
383 cacodylate buffer (EMS, Hatfield, PA, pH 7.4) followed by 30 ml fixative mixture containing 0.08
384 M cacodylate (pH 7.4), 2.5% paraformaldehyde (EMS), 1.25% glutaraldehyde (EMS) and 2 mM
385 calcium chloride (Sigma). The perfusion solution was based on the work of (Hua et al., 2015).
386 Once the brain was removed it was placed into the same fixative solution to post-fix for 16 to 72
387 hours at 4 °C.

388 After perfusion of the animals and excision of the brain, the surface of the cortex was
389 imaged using differential contrast lighting to visualize the surface vasculature of visual cortex and
390 identify the region where the cranial window had previously been. This region was then prepared
391 for Electron Microscopy. Details of the procedures to carefully map the neurophysiology site in
392 the histological sections is described in (details in ⁹). We omitted these details here as no
393 neurophysiology data was used in this manuscript, even though the anatomical data originates from
394 the same block of tissue that was recorded with two-photon imaging. The brain was washed in CB
395 (0.1 M cacodylate buffer pH 7.4) and embedded in 2% agarose. The agarose was trimmed and
396 mounted for coronal sectioning in a Leica VT1000S vibratome; successive 200 µm thick slices
397 were taken until the entire region of cortical tissue previously demarcated by manual markings
398 was sectioned. During this procedure, we also acquired blockface images of each brain slice. The
399 coronal sections containing the imaged site were then selected for histological processing (see
400 below).

401

402 **EM Histology**

403 The histology protocol used here is based on the work of ⁶¹ and ⁶², with modifications to
404 accommodate different tissue block sizes and to improve tissue contrast for transmission electron
405 microscopy (TEM). Following several washes in CB (0.1 M cacodylate buffer pH 7.4), the
406 vibratome slices were treated with a heavy metal staining protocol. Initial osmium fixation with
407 2% osmium tetroxide in CB for 90 minutes at room temperature was followed by immersion in
408 2.5% potassium ferricyanide in CB for 90 minutes at room temperature. After 2 x 30 minute
409 washes with deionized (DI) water, the tissue was treated with freshly made and filtered 1% aqueous
410 thiocarbohydrazide at 40 °C for 10 minutes. The samples were washed 2 x 30 minutes with DI
411 water and treated again with 2% osmium tetroxide in water for 30 minutes at room temperature.
412 Double washes in DI water for 30 min each were followed by immersion in 1% aqueous uranyl
413 acetate overnight at 4°. The next morning, the samples in the same solution were placed in a heat
414 block to raise the temperature to 50° for 2 hours. The samples were washed twice in DI water for
415 30 minutes each, then incubated in Walton's lead aspartate pH 5.0 for 2 hours at 50 °C in the heat
416 block. After double washes in DI water for 30 minutes each, the slices were dehydrated in an
417 ascending ethanol series (50%, 70%, 90%, 3 x 100%) 10 minutes each and two transition fluid
418 steps of 100 % acetonitrile for 20 minutes each. Infiltration with acetonitrile:resin dilutions at
419 2p:1p (24 h), 1p:1p (48 h) and 1p:2p (24 h) were performed on a gyratory shaker. Samples were
420 placed in 100% resin for 24 hours, followed by embedment in Hard Plus resin (EMS, Hatfield,
421 PA). The samples were cured in a 60 °C oven for 96 hours.

422 In order to evaluate the quality of samples during protocol development and before preparation for
423 large scale sectioning, the following procedure was used for tissue mounting, sectioning and
424 imaging. We evaluated each sample for membrane integrity, overall contrast and quality of
425 ultrastructure. For general tissue evaluation, adjacent slices and tissue sections from the opposite

426 hemisphere, processed in the same manner as the ROI slice, were cross-sectioned and thin sections
427 were taken for evaluation of staining throughout the block neighboring the region of interest.
428

429 **Ultrathin Sectioning**

430 The tissue block was trimmed to contain the neurophysiology recording site which is the region of
431 interest (ROI) then sectioned to 40 nm ultrathin sections. For both trimming and sectioning a Leica
432 EM UC7 ultramicrotome was equipped with a diamond trimming tool and an Ultra 35 diamond
433 knife (Diatome USA) respectively. Sectioning speed was set to 0.3 mm/sec. Eight to ten serial thin
434 sections were cut to form a ribbon, after which the microtome thickness setting was changed to 0
435 nm in order to release the ribbon from the knife edge. Then, using an eyelash superglued to a
436 handle, ribbons were organized to pairs and picked up as pairs to copper grids (Pelco, SynapTek,
437 1.5 mm slot hole) covered by 50nm thick LUXFilm support (Luxel Corp., Friday Harbor, WA).
438

439 **Electron microscopy imaging**

440 The imaging platform used for high throughput serial section imaging is a JEOL-1200EXII 120kV
441 transmission electron microscope that has been modified with an extended column, a custom
442 scintillator, and a large format sCMOS camera outfitted with a low distortion lens. The column
443 extension and scintillator facilitate an estimated 10-fold magnification of the nominal field of view
444 with negligible impact on resolution. Subsequent imaging of the scintillator with a high-resolution,
445 large-format camera allows the capture of fields-of-view as large as 13x13 μm at 4 nm resolution.
446 As with any magnification process, the electron density at the phosphor drops off as the column is
447 extended. To mitigate the impact of reduced electron density on image quality (shot noise), a high-
448 sensitivity sCMOS camera was selected and the scintillator composition tuned in order to generate
449 high quality EM images within exposure times of 90 - 200 ms⁶³.
450

451 **Image volume assembly and morphological segmentation**

452 Aligning the individual image tiles and sections into a coherent three-dimensional volume and
453 segmenting the cellular morphology for the P36 dataset was performed as previously described
454 within⁹⁻¹¹.
455

456 **Proofreading and Annotation of Volumetric Imagery Data**

457 We used a combination of Neuroglancer (Maitin-Shepard,
458 <https://github.com/google/neuroglancer>) and custom tools to annotate and store labeled spatial
459 points⁶⁴. In brief, we used Neuroglancer to simultaneously visualize the imagery and segmentation
460 of the 3d EM data. A custom branch of Neuroglancer was developed that could interface with a
461 “dynamic” segmentation database, allowing users to correct errors (i.e., either merging or splitting
462 neurons) in a centralized database from a web browser. Neuroglancer has some annotation
463 functionality, allowing users to place simple annotations during a session, but does not offer a way
464 to store them in a central location for analysis. We thus built a custom cloud-based database system
465 to store arbitrary annotation data centered associated with spatial points that could be propagated
466 dynamically across proofreading events. Annotations were programmatically added to the
467 database using a custom python client and, in relevant cases, after parsing temporary Neuroglancer
468 session states using custom python scripts. These spatial points and their associated data (e.g.,
469 synapse type, cell body ID number, or cell types) were linked to stored snapshots of the
470 proofreading for querying and reproducible data analysis. All data analyzed here came from the
471 “v183” snapshot.

472

473 **Visualization and Analysis of Mesh Data**

474 Neuronal meshes were computed by Igneous (<https://github.com/seung-lab/igneous>) and kept up
475 to date across proofreading. Meshes were analyzed in a custom python library, MeshParty
476 (<https://github.com/sdorkenw/MeshParty>), that extends Trimesh (<https://trimsh.org>) with domain-
477 specific features and VTK (<https://www.vtk.org>) integration for visualization. In cases where
478 skeletons were used, we computed them with a custom modification of the TEASAR algorithm⁶⁵
479 on the vertex adjacency graph of the mesh object implemented as part of MeshParty. In order to
480 associate annotations such as synapses or AIS boundary points with a mesh, we mapped point
481 annotations to the closest mesh vertex after removing artifacts from the meshing process.

482

483 **Quantification and Statistical Analysis**

484 A t-test (two sample assuming unequal variance, two tailed) was performed in Microsoft Excel
485 to compare number and densities of phagolysosomes. Measurements were taken from different
486 cells.

487

488 **Annotation of cells in the EM volume**

489 We used a combination of Neuroglancer (Maitin-Shepard <https://github.com/google/neuroglancer>)
490 and custom tools to annotate and store labeled spatial points. In brief, we used Neuroglancer to
491 simultaneously visualize the imagery and segmentation of the 3d EM data. Neuroglancer
492 incorporates the capability to store and remark on xyz points within the data. These spatial points
493 and their associated data (e.g., Cell type, cell body ID number, or organelles) were linked to stored
494 spreadsheets and documents.

495

496 **Mouse primary OPC culture**

497 Cerebral cortices from post-natal day 6 or 7 (P6/P7) CD1 mouse pups (Charles River) were
498 collected, and tissue was dissociated using MACS Milltenyi Biotec Neural Tissue Dissociation Kit
499 (P) (130-092-628), according to the manufacturer's instructions. Briefly, cortices were collected
500 from each pup and incubated at 37°C with gentle rotation using a MACSmix™ Tube Rotator (130-
501 090-753) following digestion with pre-warmed enzyme P mix. Cells were then mechanically
502 dissociated and passed through a 70µm MACS SmartStrainer and a 70µm Pre-Separation Filter to
503 remove cell clumps before incubation with Anti-O4 Microbeads (130-094-543). Cells were then
504 loaded into an MS column (130-042-201) in for magnetic separation, and positively-selected cells
505 were collected following extrusion through the column.

506

507 Cells were plated at a density of about 20,000 cells / well in a 24-well plate with 1.5mm coverslips
508 in each well that had previously been coated overnight with poly-d-lysine (50µL PDL in 250mL
509 dH₂O). Cells were expanded overnight at 37°C in OPC media containing recombinant human
510 PDGF-AA and Neurotrophin-3 until optimal density was reached. The plates were then processed
511 for immunofluorescence staining.

512

513 **Staining of primary OPC cultures**

514 Coverslips were washed once with 1x PBS before 4% PFA was applied for 13 minutes at room
515 temperature. Cells were then washed twice with 1x PBS (5 minutes/wash) before blocking in 0.5%
516 Saponin, 5% normal donkey serum, and 1x PBS) for 1 hour at room temperature. Cells were then
517 stained with primary antibodies against NG2 proteoglycan (guinea pig, 1:100, custom Bergles

518 antibody), LAMP2 (rat, Abcam, 1:200) to visualize OPC cell bodies/ processes and lysosomes,
519 respectively. Following overnight incubation at 4°C with rotation, cells were washed three times
520 with 1x PBS (5 minutes/wash) at room temperature. AlexaFluor secondary antibodies (488 donkey
521 anti-rat and 647 donkey anti-guinea pig) were applied for 1 hour at room temperature in the dark.
522 Cells were again washed three times, DAPI stain was applied for 10 minutes, and cells were
523 washed again twice before coverslips were removed and mounted to slides using ProLong™ Gold
524 Antifade Mountant and allowed to dry at room temperature for 24 hours.
525

526 **Imaging and analysis of primary OPC cultures**

527 Cells from three separate culture experiments were used for the analysis. All images were taken
528 at 63x magnification using the AiryScan function on a Zeiss 710 confocal microscope. Airyscan-
529 processed z-stacks of NG2⁺ individual OPCs were projected using the maximum intensity
530 projection function, and the number of LAMP2⁺ vesicles within cell processes were quantified.
531

532 **Reagents used in primary OPC cultures**

533 *OPC Culture Tools – all Miltenyi* (Cat no.)

534 MACS Miltenyi Biotec Neural Tissue Dissociation Kit (P) (130-092-628)

535 MACS Miltenyi Biotec Anti-O4 MicroBeads (130-094-543)

536 MACS SmartStrainer (70µm) (130-090-753)

537 MACSmix™ Tube Rotator (130-090-753)

538 Pre-Separation Filters, 70µm (130-095-823)

539 MACS MS Columns (130-042-201)

540 MACS Multistand (130-042-303)

541 MiniMACS™ Separator (130-042-102)

542

543 **Antibodies**

544 Anti-NG2 (Guinea pig, source: Bergles Laboratory)

545 Anti-LAMP2 (Abcam, cat no. ab13524)

546

547 **Additional Reagent**

548 0.5% saponin (Millipore Sigma, 47036)

549 ProLong™ Gold Antifade Mountant (ThermoFisher, cat no. P10144)

550

551 **Experimental Models: Organisms/ Strains**

552 CD1 mice, Charles River (Strain number 022)

553

554 **Molecular analysis of OPCs and microglia with single nucleus RNA-seq and single nucleus 555 DNA methyl-seq2 dataset.**

556 We analyzed recently described Chromium 10x V3 single nucleus RNA-seq and single nucleus
557 DNA methyl-seq2 datasets from mouse primary motor cortex³⁵, available from the Neuroscience
558 Multi-omic Data Archive (NeMO, <https://assets.nemoarchive.org/dat-ch1nqb7>). Only the
559 159,738 nuclei from the dataset generated by the Broad Institute were used.

560 For gene expression dot plots, the mean UMIs per cluster and proportion of cluster with UMIs
561 greater than 1 were calculated using the scratth.hicat v0.0.22 library

562 (<https://github.com/AllenInstitute/sratth.hicat>) and visualized using ggplots2 v3.3.3 library⁶⁶ in

563 R v3.4.1. Mean expression was scaled from 0 to 1 for each gene for each major cell class (i.e.

564 non-neuronal and neurons). To find neuronal subclass marker genes, we first created a Seurat⁶⁷,
565 ⁶⁸ object of only the neuronal cell types, downsampled to 500 nuclei per neuronal subclass. We
566 then used the FindAllMarkers function from Seurat v3.2.0 with the ‘roc’ test to identify
567 differentially expressed genes that were enriched in a particular neuronal subclass compared to
568 other neurons. Neuronal subclass marker genes were then filtered to include genes with greater
569 than 2 log₂FC in OPCs and microglia relative to each mature oligodendrocyte cluster (Oligo
570 Opalin_1-3), and with greater than 2 log₂ cpm expression in OPCs and microglia.
571 To visualize single nucleus DNA methyl-seq₂ tracks, we loaded gene body methylation (CGN)
572 tracks into the UCSC genome browser. Example tracks of neuronal subclass marker genes that
573 showed expression in OPCs were identified to highlight the lack of DNA hypomethylation in
574 OPCs.

575 Specific GO term gene lists for lysosome, phagocytosis, and synapse assembly were
576 downloaded from <http://www.informatics.jax.org/go/term/> on January 20th, 2021^{69,70,71}. Each
577 gene list was filtered to include genes with greater than 2 log₂FC in OPCs and/or microglia
578 relative to each mature oligodendrocyte cluster, and with greater than 2 log₂ cpm expression in
579 OPCs and/or microglia.

580

581 **Data availability**

582 The raw images, segmentation, and synaptic connectivity will be made available upon or before
583 publication.

584 Code availability

585 All software is open source and available at <http://github.com/seung-lab> if not otherwise
586 mentioned.

587 Alembic: Stitching and alignment.

588 CloudVolume: Reading and writing volumetric data, meshes, and skeletons to and from the
589 cloud

590 Chunkflow: Running convolutional nets on large datasets

591 DeepEM: Training convolutional nets to detect neuronal boundaries.

592 DynamicAnnotationFramework: Proofreading and connectome updates

593 (visit <https://github.com/seung-lab/AnnotationPipelineOverview> for repository list)

594 Igneous: Coordinating downsampling, meshing, and data management.

595 MeshParty: Interaction with meshes and mesh-based skeletonization

596 (<https://github.com/sdorkenw/MeshParty>)

597 MMAAPP: Watershed, size-dependent single linkage clustering, and mean affinity
598 agglomeration.

599 PyTorchUtils: Training convolutional nets for synapse detection and partner assignment

600 (<https://github.com/nicholasturner1/PyTorchUtils>).

601 Synaptor: Processing output of the convolutional net for predicting synaptic clefts

602 (<https://github.com/nicholasturner1/Synaptor>).

603 TinyBrain and zmesh: Downsampling and meshing (precursors of the libraries that were used).

604

605

606

607

608

609

References

- 611
612
- 613 1 Pan, Y. & Monje, M. Activity Shapes Neural Circuit Form and Function: A Historical
614 Perspective. *J Neurosci* **40**, 944-954, doi:10.1523/JNEUROSCI.0740-19.2019 (2020).
- 615 2 Schafer, D. P. *et al.* Microglia sculpt postnatal neural circuits in an activity and
616 complement-dependent manner. *Neuron* **74**, 691-705, doi:10.1016/j.neuron.2012.03.026 (2012).
- 617 3 Chung, W. S. *et al.* Astrocytes mediate synapse elimination through MEGF10 and
618 MERTK pathways. *Nature* **504**, 394-400, doi:10.1038/nature12776 (2013).
- 619 4 Raff, M. C., Miller, R. H. & Noble, M. A glial progenitor cell that develops in vitro into
620 an astrocyte or an oligodendrocyte depending on culture medium. *Nature* **303**, 390-396,
621 doi:10.1038/303390a0 (1983).
- 622 5 Baxi, E. G. *et al.* Lineage tracing reveals dynamic changes in oligodendrocyte precursor
623 cells following cuprizone-induced demyelination. *Glia* **65**, 2087-2098, doi:10.1002/glia.23229
624 (2017).
- 625 6 Bergles, D. & Jahr, C. E. Glutamatergic synapses on oligodendrocyte precursor cells in
626 the hippocampus. *Nature* **405**, doi:0.1016/s0896-6273(00)80420-1
627 (1997).
- 628 7 Lin, S. C. & Bergles, D. E. Synaptic signaling between neurons and glia. *Glia* **47**, 290-
629 298, doi:10.1002/glia.20060 (2004).
- 630 8 Bergles, D. E. & Richardson, W. D. Oligodendrocyte Development and Plasticity. *Cold*
631 *Spring Harb Perspect Biol* **8**, a020453, doi:10.1101/cshperspect.a020453 (2015).
- 632 9 Dorkenwald, S. *et al.* Binary and analog variation of synapses between cortical pyramidal
633 neurons
634 . *bioRxiv*, doi:10.1101/2019.12.29.890319 (2019).
- 635 10 Schneider-Mizell, C. M. *et al.* Chandelier cell anatomy and function reveal a variably
636 distributed but common signal. *bioRxiv*, doi:10.1101/2020.03.31.018952 (2020).
- 637 11 Turner, N. L. *et al.* Multiscale and multimodal reconstruction of cortical structure and
638 function. *bioRxiv*, doi:10.1101/2020.10.14.338681 (2020).
- 639 12 Motta, A. *et al.* Dense connectomic reconstruction in layer 4 of the somatosensory cortex.
640 *Science* **366**, doi:10.1126/science.aay3134 (2019).
- 641 13 Mori, S. & Leblond, C. P. Electron microscopic identification of three classes of
642 oligodendrocytes and a preliminary study of their proliferative activity in the corpus callosum of
643 young rats. *J Comp Neurol* **139**, 1-28, doi:10.1002/cne.901390102 (1970).
- 644 14 Dawson, M. R. L., J.M.; Reynolds, R. NG2-expressing cells in the CNS. *J. Neurosci res*
645 **61**, 471-479, doi:DOI: 10.1002/1097-4547(20000901)61:5<471::AID-JNR1>3.0.CO;2-N

- 646 (2000).
- 647 15 Ong, W. Y. & Levine, J. M. A light and electron microscopic study of NG2 chondroitin
648 sulfate proteoglycan-positive oligodendrocyte precursor cells in the normal and kainate-lesioned
649 rat hippocampus. *Neuroscience* **92**, 83-95, doi:10.1016/s0306-4522(98)00751-9 (1999).
- 650 16 Peters, A. A fourth type of neuroglial cell in the adult central nervous system. *Journal of*
651 *Neurocytology* **33**, 345-357, doi:https://doi.org/10.1023/B:NEUR.0000044195.64009.27
652 (2004).
- 653 17 Vaughn, J. E., Hinds, P. L. & Skoff, R. P. Electron microscopic studies of Wallerian
654 degeneration in rat optic nerves. I. The multipotential glia. *J Comp Neurol* **140**, 175-206,
655 doi:10.1002/cne.901400204 (1970).
- 656 18 Butt, A. M. *et al.* Cells expressing the NG2 antigen contact nodes of Ranvier in adult
657 CNS white matter. *Glia* **26**, 84-91 (1999).
- 658 19 Bushong, E. A., Martone, M. E., Jones, Y. Z. & Ellisman, M. H. *Protoplasmic astrocytes*
659 *in CA1 stratum radiatum occupy separate anatomical domains*. Vol. 22 (2002).
- 660 20 Nimmerjahn, A., Kirchhoff, F. & Helmchen, F. Resting microglial cells are highly
661 dynamic surveillants of brain parenchyma in vivo. *Science* **308**, 1314-1318,
662 doi:10.1126/science.1110647 (2005).
- 663 21 Ventura, R. & Harris, K. M. Three-Dimensional Relationships between Hippocampal
664 Synapses and Astrocytes. *The Journal of Neuroscience* **19**, 6897-6906, doi:10.1523/jneurosci.19-
665 16-06897.1999 (1999).
- 666 22 Schafer, D. P., Lehrman, E. K. & Stevens, B. The "quad-partite" synapse: microglia-
667 synapse interactions in the developing and mature CNS. *Glia* **61**, 24-36, doi:10.1002/glia.22389
668 (2013).
- 669 23 Battefeld, A., Klooster, J. & Kole, M. H. Myelinating satellite oligodendrocytes are
670 integrated in a glial syncytium constraining neuronal high-frequency activity. *Nat Commun* **7**,
671 11298, doi:10.1038/ncomms11298 (2016).
- 672 24 Wogram, E. *et al.* Satellite microglia show spontaneous electrical activity that is
673 uncorrelated with activity of the attached neuron. *Eur J Neurosci* **43**, 1523-1534,
674 doi:10.1111/ejn.13256 (2016).
- 675 25 Hughes, E. G., Kang, S. H., Fukaya, M. & Bergles, D. E. Oligodendrocyte progenitors
676 balance growth with self-repulsion to achieve homeostasis in the adult brain. *Nat Neurosci* **16**,
677 668-676, doi:10.1038/nn.3390 (2013).
- 678 26 Kinchen, J. M. & Ravichandran, K. S. Phagosome maturation: going through the acid
679 test. *Nat Rev Mol Cell Biol* **9**, 781-795, doi:10.1038/nrm2515 (2008).

- 680 27 Levin, R., Grinstein, S. & Canton, J. The life cycle of phagosomes: formation,
681 maturation, and resolution. *Immunol Rev* **273**, 156-179, doi:10.1111/imr.12439 (2016).
- 682 28 Tremblay, M. E., Lowery, R. L. & Majewska, A. K. Microglial interactions with
683 synapses are modulated by visual experience. *PLoS Biol* **8**, e1000527,
684 doi:10.1371/journal.pbio.1000527 (2010).
- 685 29 Huynh, K. K. *et al.* LAMP proteins are required for fusion of lysosomes with
686 phagosomes. *EMBO J* **26**, 313-324, doi:10.1038/sj.emboj.7601511 (2007).
- 687 30 Sipe, G. O. *et al.* Microglial P2Y₁₂ is necessary for synaptic plasticity in mouse visual
688 cortex. *Nat Commun* **7**, 10905, doi:10.1038/ncomms10905 (2016).
- 689 31 Paolicelli, R. C. *et al.* Synaptic pruning by microglia is necessary for normal brain
690 development. *Science* **333**, 1456-1458, doi:10.1126/science.1202529 (2011).
- 691 32 Peri, F. & Nusslein-Volhard, C. Live imaging of neuronal degradation by microglia
692 reveals a role for v0-ATPase a1 in phagosomal fusion in vivo. *Cell* **133**, 916-927,
693 doi:10.1016/j.cell.2008.04.037 (2008).
- 694 33 Espinosa, J. S. & Stryker, M. P. Development and plasticity of the primary visual cortex.
695 *Neuron* **75**, 230-249, doi:10.1016/j.neuron.2012.06.009 (2012).
- 696 34 Yoshimura, K. & Takeda, S. Hedgehog signaling regulates myelination in the peripheral
697 nervous system through primary cilia. *Differentiation* **83**, S78-85, doi:10.1016/j.diff.2011.10.006
698 (2012).
- 699 35 Yao, Z. *et al.* A taxonomy of transcriptomic cell types across the isocortex and
700 hippocampal formation. *Cell*, 2020.2003.2030.015214, doi:10.1016/j.cell.2021.04.021 (2021).
- 701 36 Mo, A. *et al.* Epigenomic Signatures of Neuronal Diversity in the Mammalian Brain.
702 *Neuron* **86**, 1369-1384, doi:10.1016/j.neuron.2015.05.018 (2015).
- 703 37 Schneble, N. *et al.* The protein-tyrosine phosphatase DEP-1 promotes migration and
704 phagocytic activity of microglial cells in part through negative regulation of fyn tyrosine kinase.
705 *Glia* **65**, 416-428, doi:10.1002/glia.23100 (2017).
- 706 38 Fernandez-Castaneda, A. *et al.* The active contribution of OPCs to neuroinflammation is
707 mediated by LRP1. *Acta Neuropathol* **139**, 365-382, doi:10.1007/s00401-019-02073-1 (2020).
- 708 39 Fitzer-Attas, C. J. *et al.* Fcγ receptor-mediated phagocytosis in macrophages
709 lacking the Src family tyrosine kinases Hck, Fgr, and Lyn. *J Exp Med* **191**, 669-682,
710 doi:10.1084/jem.191.4.669 (2000).
- 711 40 Suzuki, J., Imanishi, E. & Nagata, S. Exposure of phosphatidylserine by Xk-related
712 protein family members during apoptosis. *J Biol Chem* **289**, 30257-30267,
713 doi:10.1074/jbc.M114.583419 (2014).

714 41 Simons, M. & Nave, K. A. Oligodendrocytes: Myelination and Axonal Support. *Cold*
715 *Spring Harb Perspect Biol* **8**, a020479, doi:10.1101/cshperspect.a020479 (2015).

716 42 Snaidero, N. & Simons, M. Myelination at a glance. *J Cell Sci* **127**, 2999-3004,
717 doi:10.1242/jcs.151043 (2014).

718 43 Micheva, K. D. *et al.* A large fraction of neocortical myelin ensheathes axons of local
719 inhibitory neurons. *Elife* **5**, doi:10.7554/eLife.15784 (2016).

720 44 Stogsdill, J. A. & Eroglu, C. The interplay between neurons and glia in synapse
721 development and plasticity. *Curr Opin Neurobiol* **42**, 1-8, doi:10.1016/j.conb.2016.09.016
722 (2017).

723 45 Wu, X. *et al.* GABA signaling promotes synapse elimination and axon pruning in
724 developing cortical inhibitory interneurons. *J Neurosci* **32**, 331-343,
725 doi:10.1523/JNEUROSCI.3189-11.2012 (2012).

726 46 Raiders, S. *et al.* Engulfed by Glia: Glial Pruning in Development, Function, and Injury
727 across Species. *J Neurosci*, doi:10.1523/JNEUROSCI.1660-20.2020 (2021).

728 47 Bishop, D. L., Misgeld, T., Walsh, M. K., Gan, W. B. & Lichtman, J. W. Axon branch
729 removal at developing synapses by axosome shedding. *Neuron* **44**, 651-661,
730 doi:10.1016/j.neuron.2004.10.026 (2004).

731 48 Sierra, A., Abiega, O., Shahraz, A. & Neumann, H. Janus-faced microglia: beneficial and
732 detrimental consequences of microglial phagocytosis. *Front Cell Neurosci* **7**, 6,
733 doi:10.3389/fncel.2013.00006 (2013).

734 49 Lee, J. H. *et al.* Astrocytes phagocytose adult hippocampal synapses for circuit
735 homeostasis. *Nature*, doi:10.1038/s41586-020-03060-3 (2020).

736 50 Lim, T. K. & Ruthazer, E. S. Microglial trogocytosis and the complement system
737 regulate axonal pruning in vivo. *Elife* **10**, doi:10.7554/eLife.62167 (2021).

738 51 Tan, A. M., Zhang, W. & Levine, J. M. NG2: a component of the glial scar that inhibits
739 axon growth. *J Anat* **207**, 717-725, doi:10.1111/j.1469-7580.2005.00452.x (2005).

740 52 Hesp, Z. C. *et al.* Proliferating NG2-Cell-Dependent Angiogenesis and Scar Formation
741 Alter Axon Growth and Functional Recovery After Spinal Cord Injury in Mice. *J Neurosci* **38**,
742 1366-1382, doi:10.1523/JNEUROSCI.3953-16.2017 (2018).

743 53 Jin, X., Riew, T. R., Kim, H. L., Choi, J. H. & Lee, M. Y. Morphological characterization
744 of NG2 glia and their association with neuroglial cells in the 3-nitropropionic acid-lesioned
745 striatum of rat. *Sci Rep* **8**, 5942, doi:10.1038/s41598-018-24385-0 (2018).

746 54 Kirby, L. *et al.* Oligodendrocyte precursor cells present antigen and are cytotoxic targets
747 in inflammatory demyelination. *Nat Commun* **10**, 3887, doi:10.1038/s41467-019-11638-3
748 (2019).

749 55 Falcao, A. M. *et al.* Disease-specific oligodendrocyte lineage cells arise in multiple
750 sclerosis. *Nat Med* **24**, 1837-1844, doi:10.1038/s41591-018-0236-y (2018).

751 56 Barres, B. A. & Raff, M. C. Axonal control of oligodendrocyte development. *J Cell Biol*
752 **147**, 1123-1128, doi:10.1083/jcb.147.6.1123 (1999).

753 57 Tomassy, G. S. *et al.* Distinct profiles of myelin distribution along single axons of
754 pyramidal neurons in the neocortex. *Science* **344**, 319-324, doi:10.1126/science.1249766 (2014).

755 58 Timmler, S. & Simons, M. Grey matter myelination. *Glia* **67**, 2063-2070,
756 doi:10.1002/glia.23614 (2019).

757 59 Wake, H. *et al.* Nonsynaptic junctions on myelinating glia promote preferential
758 myelination of electrically active axons. *Nat Commun* **6**, 7844, doi:10.1038/ncomms8844 (2015).

759 60 Madisen, L. *et al.* Transgenic mice for intersectional targeting of neural sensors and
760 effectors with high specificity and performance. *Neuron* **85**, 942-958,
761 doi:10.1016/j.neuron.2015.02.022 (2015).

762 61 Hua, Y., Laserstein, P. & Helmstaedter, M. Large-volume en-bloc staining for electron
763 microscopy-based connectomics. *Nat Commun* **6**, 7923, doi:10.1038/ncomms8923 (2015).

764 62 Tapia, J. C. *et al.* High-contrast en bloc staining of neuronal tissue for field emission
765 scanning electron microscopy. *Nat Protoc* **7**, 193-206, doi:10.1038/nprot.2011.439 (2012).

766 63 Yin, W. *et al.* A petascale automated imaging pipeline for mapping neuronal circuits with
767 high-throughput transmission electron microscopy. *Nat Commun* **11**, 4949, doi:10.1038/s41467-
768 020-18659-3 (2020).

769 64 Wu, J., Silversmith, W. M., Lee, K. & Seung, H. S. Chunkflow: hybrid cloud processing
770 of large 3D images by convolutional nets. *Nature Methods* **18**, 328-330, doi:10.1038/s41592-
771 021-01088-5 (2021).

772 65 M. Sato, I. B., M. A. Bender, A. E. Kaufman and M. Nakajima. TEASAR- Tree-structure
773 Extraction Algorithm for Accurate and Robust Skeletons *Proceedings the Eighth Pacific*
774 *Conference on Computer Graphics and Applications*, 281-449,
775 doi:10.1109/PCCGA.2000.883951 (2000).

776 66 Wickham, H. & Grolemund, G. *R for Data Science: Import, Tidy, Transform, Visualize,*
777 *and Model Data.* (O'Reilly Media, 2016).

778 67 Stuart, T. *et al.* Comprehensive Integration of Single-Cell Data. *Cell* **177**, 1888-1902
779 e1821, doi:10.1016/j.cell.2019.05.031 (2019).

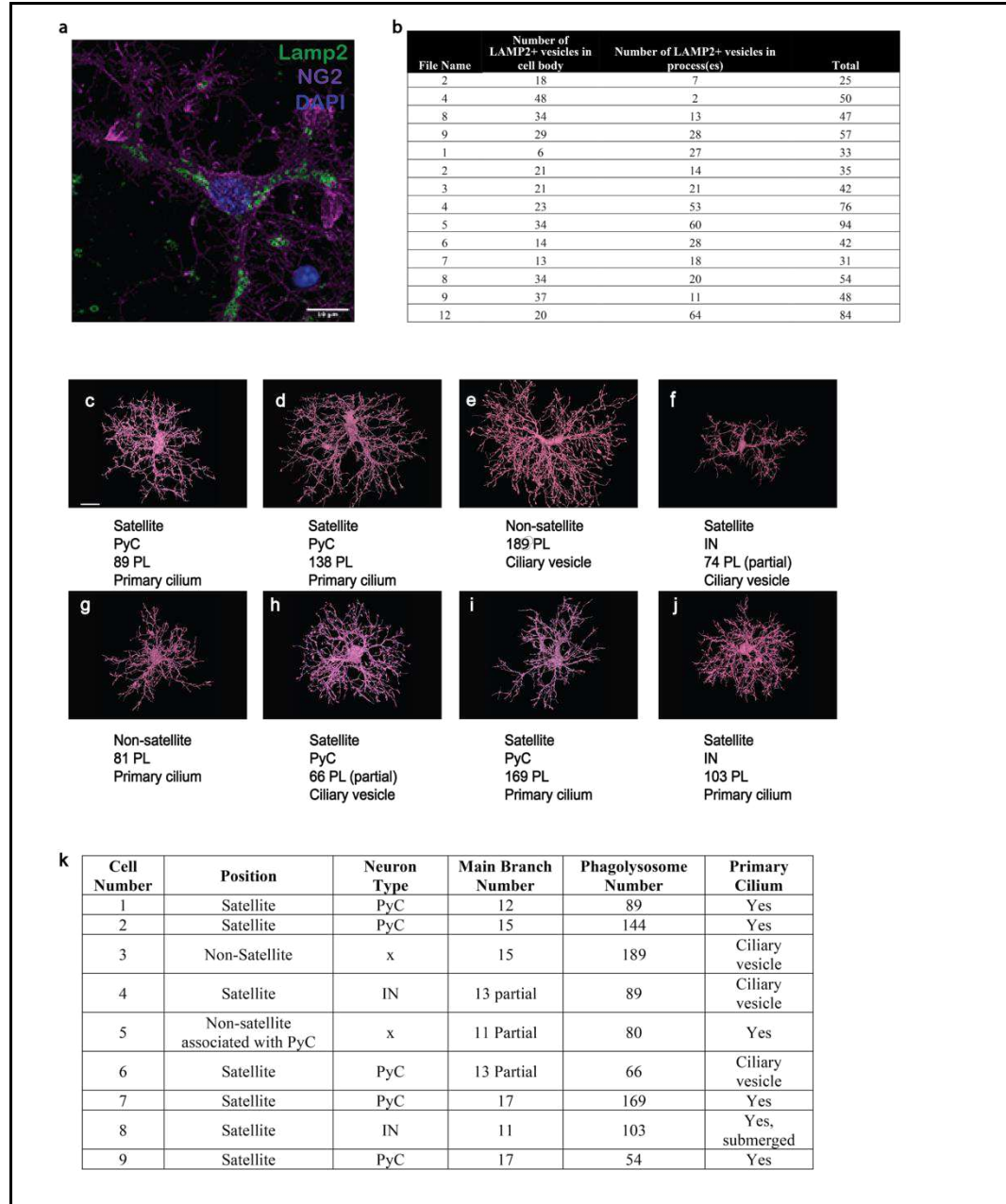
780 68 Butler, A., Hoffman, P., Smibert, P., Papalexi, E. & Satija, R. Integrating single-cell
781 transcriptomic data across different conditions, technologies, and species. *Nat Biotechnol* **36**,
782 411-420, doi:10.1038/nbt.4096 (2018).

783 69 Bult, C. J. *et al.* Mouse Genome Database (MGD) 2019. *Nucleic Acids Res* **47**, D801-
784 D806, doi:10.1093/nar/gky1056 (2019).

785 70 Smith, C. M. *et al.* The mouse Gene Expression Database (GXD): 2019 update. *Nucleic*
786 *Acids Res* **47**, D774-D779, doi:10.1093/nar/gky922 (2019).

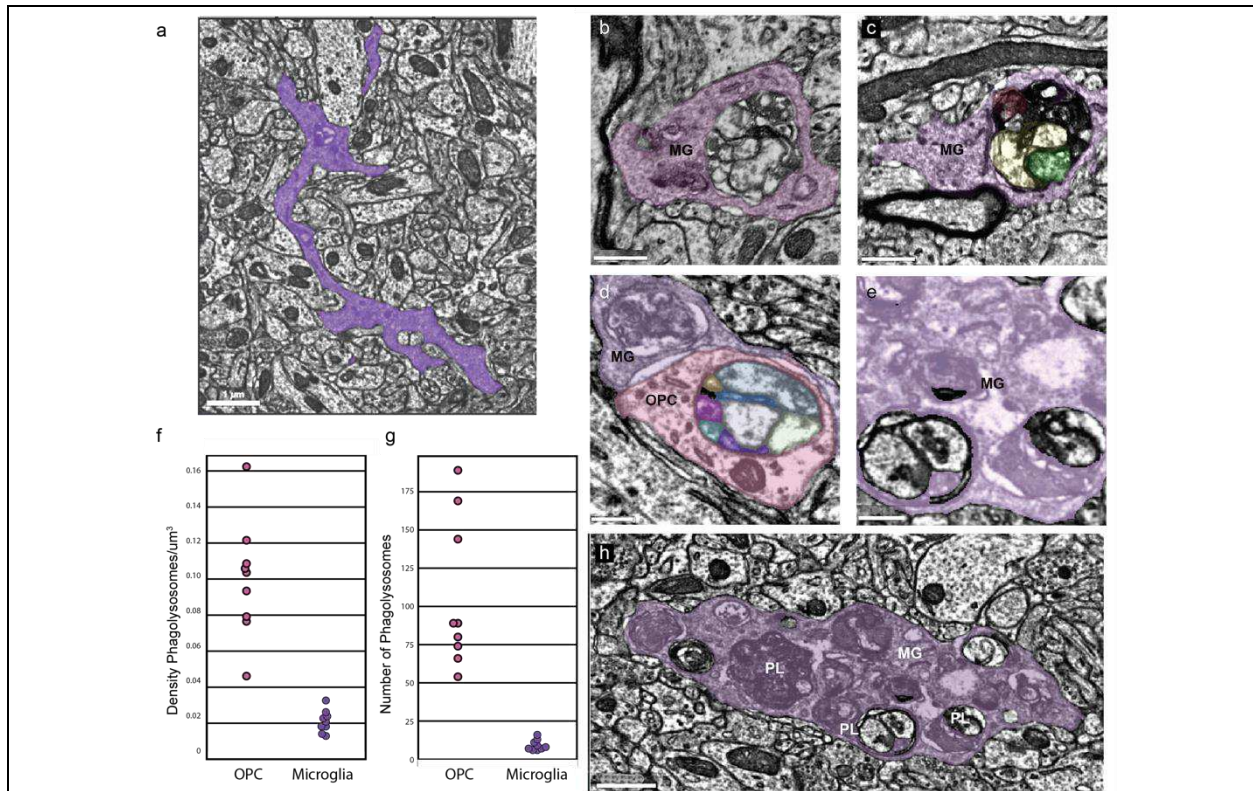
787 71 Krupke, D. M. *et al.* The Mouse Tumor Biology Database: A Comprehensive Resource
788 for Mouse Models of Human Cancer. *Cancer Res* **77**, e67-e70, doi:10.1158/0008-5472.CAN-17-
789 0584 (2017).

790
791
792
793
794
795
796



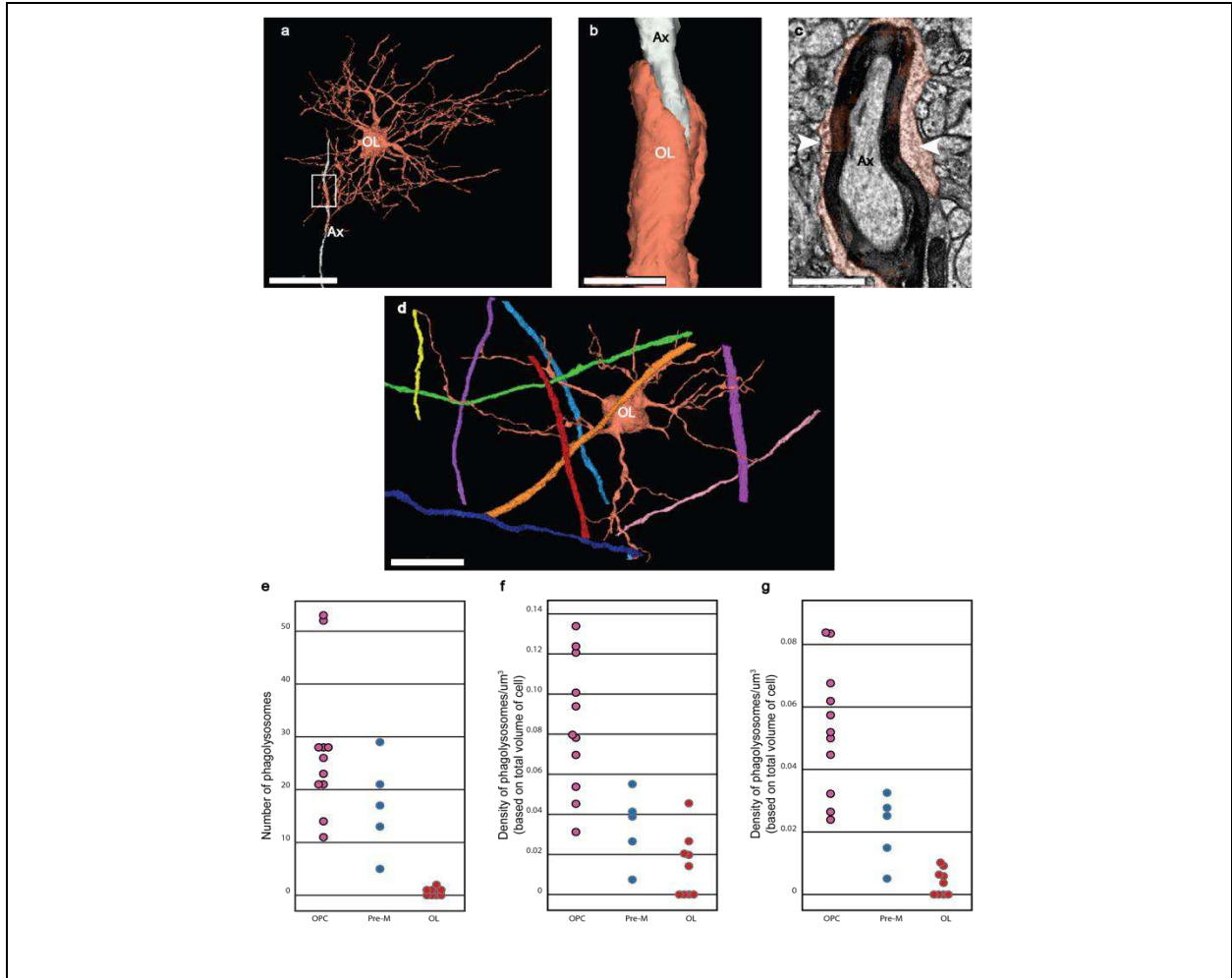
Extended data Figure 1. Phagolysosome counts and OPC features.

a, Primary cultured OPC, immunolabeled with Lamp2 (green) and NG2 chondroitin- sulfate proteoglycan (fuchsia), nucleus stained in blue (DAPI). Scale bar 10 μm. **b**, Quantification of Lamp2 positive organelles (lysosomes and phagolysosomes) in OPC soma and branches. **c-j**. Vignettes of 8 of 16 OPCs used for analysis in the P36 dataset. the ninth cell is pictured in Fig. 2a. Scale bar for all cells, 15 μm. **k**, Cells were scored for satellite position, neuron host type, number of main branches, number of phagolysosomes and presence of primary cilia.



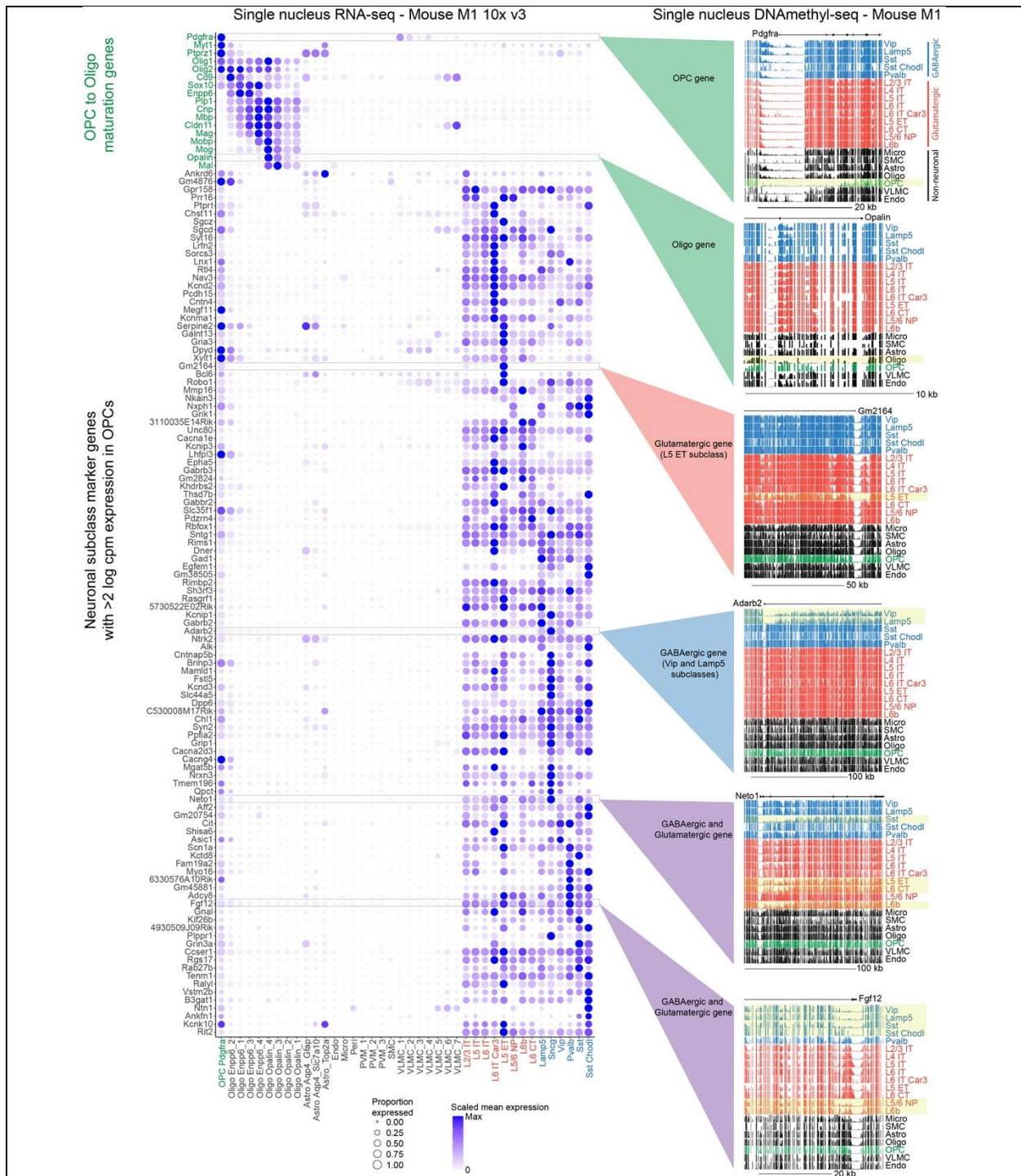
Extended Data Figure 2. Phagolysosomes in Microglia.

a, Microglial cell branch in purple shows a phagolysosome (arrow) in its dense cytoplasm. Scale bar, 1 μm . **b**, and **c**, Two large phagolysosomes from P49 dataset microglial cells (MG) in purple reveal electron dense material ingested within are in close proximity to myelinated axons (arrows). Scale bars, 500 nm. **d**, A microglial (MG) branch (purple) from P36 dataset contacts and OPC branch in pink with a phagolysosomes in both cells. Scale bar, 300 nm. **e**, A cluster of phagolysosomes in a microglial cell from P36 dataset shows electron dense material within without any sign of 40 nm vesicles. Scale bar, 300 nm. **f**, Comparison of density of phagolysosomes at P36 between OPCs and microglia (density was calculated including the volume of the soma region) **g**, Comparison of the total number of phagolysosomes at P36 between OPCs and microglia **h**, A lower magnification view of the branch in **e** shows the cytoplasm congested with phagolysosomes(PL). Scale bar, 750 nm. **f**, **g**, Plot shows the comparison of phagolysosome numbers in the microglia in P36 and P49 datasets.

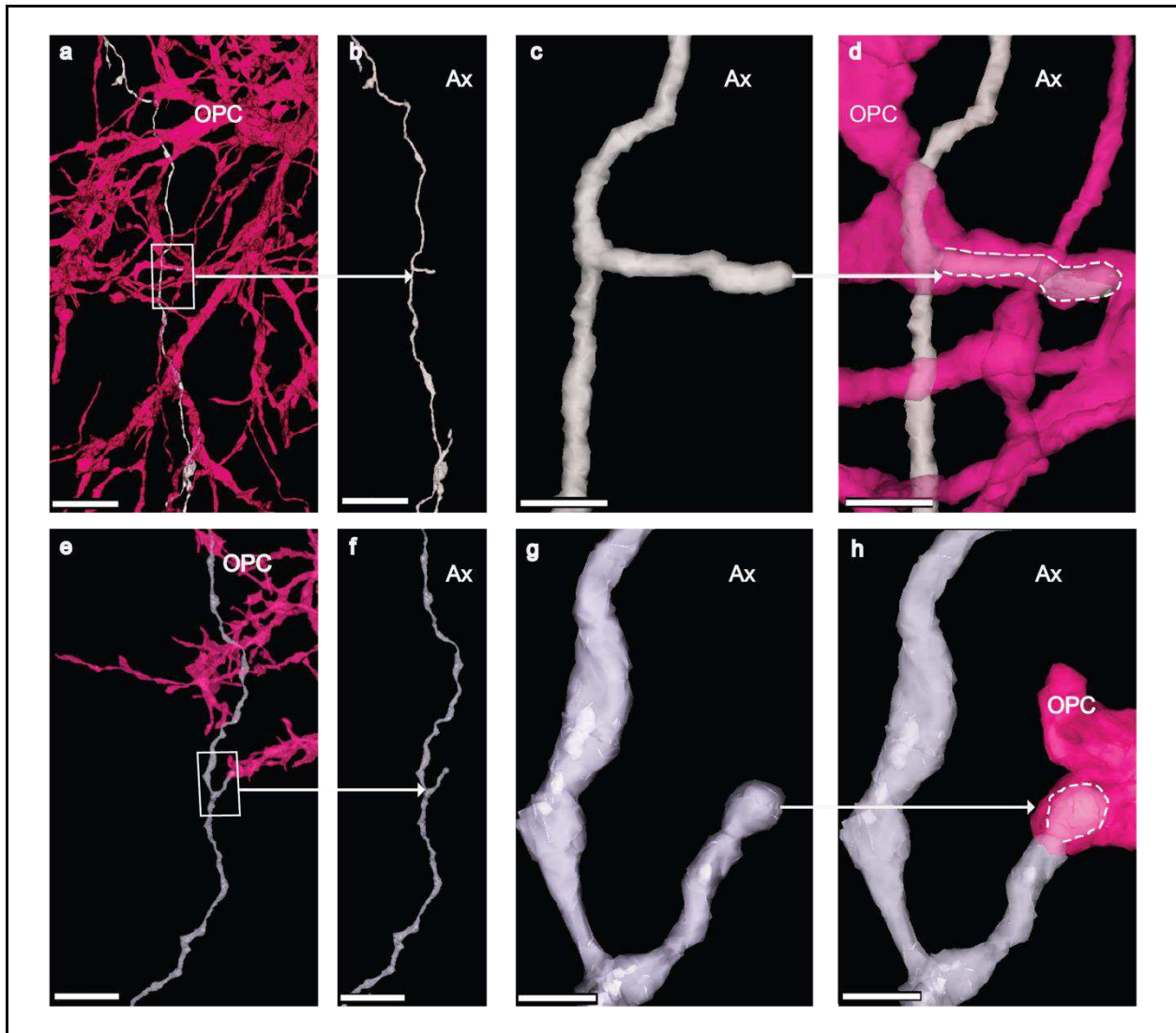


Extended data Figure 3. Premyelinating cells, myelinating oligodendrocyte and phagolysosome densities.

a, 3D rendering of a premyelinating oligodendrocyte (OL) in P49 dataset shows a branch aligned with an axon (white)(boxed area). Scale bar, 20 μm . **b**, Higher magnification view of boxed area shows myelin (orange) and axon (white). Scale bar, 1.5 μm . **c**, Ultrathin section view shows the uncompact myelin(orange)(arrows) on the outside of the compact myelin (black). Scale bar, 750 nm. **d**, Mature myelinating oligodendrocyte (OL) has thin branches that are aligned with colored myelinated axons. Scale bar, 10 μm . **e-g**, Plots comparing densities of phagolysosome distribution in OPCs, Premyelinating cells and mature oligodendrocytes.

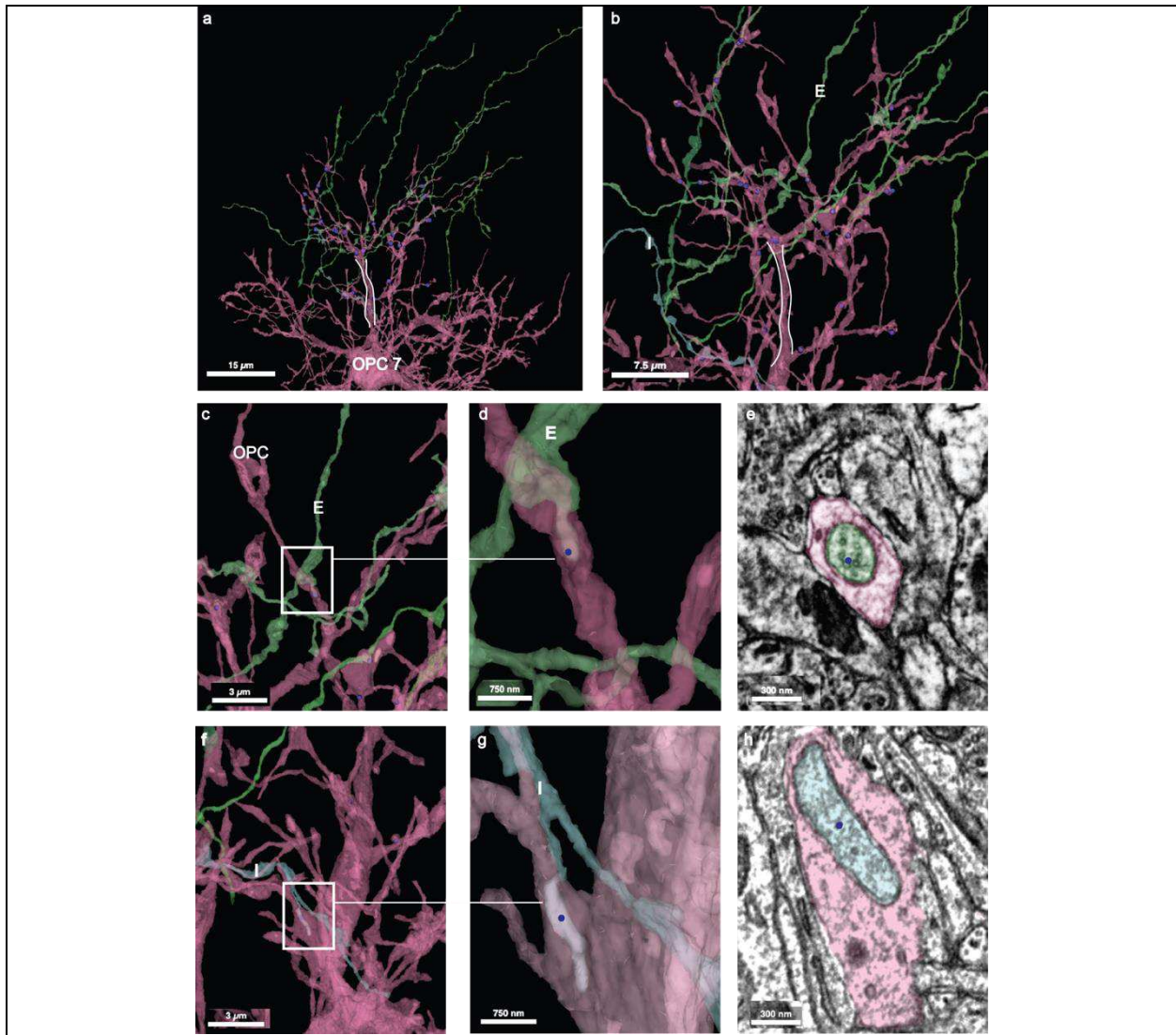


Extended Data Figure 4. Transcriptomic and epigenomic profiling of neuronal subclass genes in OPCs. Dot plot of OPC to oligodendrocyte maturation genes (green) and neuronal subclass marker genes for all non-neuronal clusters and neuronal subclasses in dataset. Expression is scaled by gene across all clusters and subclasses. Blue indicates GABAergic and red indicates glutamatergic neuronal subclasses. Clusters with of gene body DNA hypomethylation are highlighted in yellow.



Extended Figure 5. OPCs ingest collateral branches.

a, OPC (pink) contacts an excitatory axon (gray). Boxed area shows site of ingestion. Scale bar, 5 μ m. **b**, 3 D rendering of the excitatory axon (gray). Arrow points to collateral branch in boxed area in (**a**). Scale bar, 5 μ m. **c**, Higher magnification of collateral branch. White arrow points to ingested branch in (**d**). Scale bar, 750 nm. **d**, 3D rendering of excitatory axon (gray) ingested within the branch of an OPC (pink). Dotted line indicates the outline of ingested collateral branch. Scale bar, 750 nm. **e**, OPC (pink) contacts inhibitory axon (gray). Boxed area shows site of ingestion. Scale bar, 5 μ m. **f**, 3D rendering of inhibitory axon (gray). Arrow points to collateral branch in boxed area in (**e**). Scale bar, 5 μ m. **g**, Higher magnification of collateral branch. White arrow points to ingested branch in (**e**). Scale bar, 750 nm. **h**, 3D rendering of inhibitory axon (grey) ingested within the branch of an OPC (pink). Dotted line indicates the outline of ingested collateral branch. Scale bar, 750 nm. Also see supplementary video 3.



Extended Data Figure 6. Axons engulfed within OPC7 main branch .

a) One branch (while outline mark trunk) of OPC7(pink) was used to annotate axons engulfed within OPC cytoplasm. Scale bar, 15 μm . **b)** Higher magnification view of OPC branch trunk (white outline) and its processes(pink) and excitatory axons(E) in green. Scale bar, 7.5 μm . **c)** A portion of an excitatory axon(boxed area) is engulfed within the OPC cytoplasm(pink). Scale bar, 3 μm . **d,** Higher magnification view of boxed area shows engulfed tip (blue dot) of excitatory axon(E). Scale bar, 750 nm. **e,** Ultrathin section view of cross section of the green excitatory axon inside the OPC process(blue dot). Scale bar, 300 nm. **f,** A portion of an inhibitory (I) axon in blue (boxed area)is engulfed within OPC cytoplasm(pink). Scale bar, 3 μm . **g,** Higher magnification view of boxed area shows portion of the engulfed inhibitory axon branch (blue dot)within the OPC cytoplasm(pink). Scale bar, 750 nm. **h,** Ultrathin section view shows the inhibitory axon(blue dot) surrounded by OPC cytoplasm(pink). Scale bar, 300 nm.

805
806
807

Author Contributions

808 Conceptualization J.B., D.E.B., N.L. J., T.E. B., N.M.C; Software (Alignment) G.M., F.C., R.T.,
809 T.M.,W.M.S and W.W.; Software (Analysis infrastructure) C.S.J., C.S.M., F.C and S.D., S.S.;
810 Software (Data interaction and viewing) M.C., N.K. and W.M.S.; Software (Cloud data storage)
811 W.M.S.; Software Proofreading System) J.Zu., N.K. and S.D.; Formal Analysis A.N., B.H.,
812 C.S.M., F.C., J.Zh. and S.D.; Investigation (Histological preparation for EM), J.B., M.T. and
813 N.M.C.; Investigation (Sectioning sample for EM), A.A.B and A.L.B, D. J. B.; Investigation (EM
814 Imaging), W. Y., D.B., A.A.B, A.L.B, D.J.B, N.M.C and R. C. R.; Investigation (Alignment) D.I.,
815 G.M., I.T., R.T, T.M., Y. L. and W.W.; Investigation (Neuron Reconstruction) A.Z., I.T., J. Zu.,
816 J.W., K.L., M.C., N.K., R.L., S.P., S. M. and T.M.; Investigation (Synapse Detection) J.W and
817 N.L.T.; Investigation (Cell Typing): J.B, L. E., F.C., C.O., A.M.W. and N.M.C.; Data Curation
818 (Proofreading) N.M.C., Investigation (Sub cellular structures): C. O. , J.B. and J.L.-S Investigation
819 (Genomics): N.L. J., T.E. B, R. H. and E.S. L. Investigation (OPC cultures): J. G. and D. E. B.
820 Writing-original J.B., D.E.B., N.L. J., T.E. B., N.M.C. Writing – Review & Editing F.C., H.S.S.,
821 R.C.R., C. O., M. T., N. T.; Visualization C.S.M. and F.C., Supervision E.S. L., J.L.-S., D.E. B.,
822 H.S.S., N.M.C. and R.C.R., Project administration H.S.S., N.M.C. and R.C.R., Funding
823 Acquisition H.S.S., N.M.C. and R.C.R.

824

825

826 **Acknowledgments**

827 We thank John Philips, Sill Coulter and the Program Management team at the AIBS for their
828 guidance for project strategy and operations. We thank Hongkui Zeng, Christof Koch and Allan
829 Jones for their support and leadership. We thank Andreas Tolias, Jacob Reimer and their teams
830 at the Baylor College of Medicine for providing the mice used for electron microscopy. We
831 thank the Manufacturing and Processing Engineering team at the AIBS for their help in
832 implementing the EM imaging and sectioning pipeline. We thank Rob Young and the
833 Technology team at the AIBS for their work in the imaging processing of the EM data. We thank
834 Brian Youngstrom, Stuart Kendrick and the Allen Institute IT team for support with
835 infrastructure, data management and data transfer. We thank the Facilities, Finance, and Legal
836 teams at the AIBS for their support on the MICrONS contract. We thank Stephan Saalfeld for
837 help with the parameters for 2D stitching and rough alignment of the dataset. We would like to
838 thank the “Connectomics at Google” team for developing Neuroglancer and computational
839 resource donations. We also would like to thank Amazon and Intel for their assistance. We thank
840 S. Koolman, M. Moore, S. Morejohn, B. Silverman, K. Willie, and R. Willie for their image
841 analyses, Garrett McGrath for computer system administration, and May Hussein and Larry and
842 Janet Jackel for project administration. We thank Kristina Micheva and Stephen J Smith for
843 advice and feedback. We thank Profs. Joseph Ayers, Erin Cram and James Monaghan for
844 guidance, support and feedback. Supported by the Intelligence Advanced Research Projects
845 Activity (IARPA) via Department of Interior/ Interior Business Center (DoI/IBC) contract
846 numbers D16PC00003, D16PC00004, and D16PC00005. The U.S. Government is authorized to
847 reproduce and distribute reprints for Governmental purposes notwithstanding any copyright
848 annotation thereon. Disclaimer: The views and conclusions contained herein are those of the
849 authors and should not be interpreted as necessarily representing the official policies or
850 endorsements, either expressed or implied, of IARPA, DoI/IBC, or the U.S. Government. HSS
851 also acknowledges support from NIH/NINDS U19 NS104648, and research reported in this
852 publication was supported by the National Institute of Mental Health of the National Institutes of
853 Health under Award Number U19MH114824.

854
855 ARO W911NF-12-1-0594, NIH/NEI R01 EY027036, NIH/NIMH U01 MH114824, NIH/NINDS
856 R01NS104926, NIH/NIMH RF1MH117815. NIH/NIA R01AG072305 (DB), the Dr. Miriam and
857 Sheldon G Adelson Medical Research Foundation (DB), and the Mathers Foundation. The content
858 is solely the responsibility of the authors and does not necessarily represent the official views of
859 the National Institutes of Health.
860 We thank the Allen Institute for Brain Science founder, Paul G. Allen, for his vision,
861 encouragement and support.
862
863

Supplementary Files

This is a list of supplementary files associated with this preprint. Click to download.

- [mgcliptest5.mp4](#)
- [UsingNeuroglancertoAnalyseOPCsvideo2.mp4](#)
- [jbsupplmentalvideov1.mp4](#)